



---

LARGE SYNOPTIC SURVEY TELESCOPE

---

**Large Synoptic Survey Telescope (LSST)**

**LSST Crowded Fields photometry**

**K. Suberlak, C. Slater, Ž. Ivezić**

**LSST-2017**

**Latest Revision: 2018-03-06**

revision: TBD  
status: draft

## Abstract

A report on the performance of current LSST Stack pipelines in crowded stellar fields. Using the real data we explore the metrics that could be used to direct decision-making process for pipeline improvements. The quality metrics show also a way to validate the performance of LSST pipelines after major software upgrades.

Draft



## Change Record

Version	Date	Description	Owner name
1	2017-07-16	First draft.	Krzysztof Suberlak
2	2017-10-19	Updated outline.	Krzysztof Suberlak
2	2018-01-25	Major revision.	Krzysztof Suberlak

## Contents

<b>1</b>	<b>Introduction</b>	<b>1</b>
<b>2</b>	<b>Identifying density regions</b>	<b>2</b>
<b>3</b>	<b>DECam Plane Survey</b>	<b>5</b>
<b>4</b>	<b>LSST Processing of DECAPS data</b>	<b>8</b>
4.1	Cleaning DECAPS catalog, comparison to LSST pixel mask . . . . .	8
4.2	Cleaning LSST catalog . . . . .	9
<b>5</b>	<b>Metrics</b>	<b>16</b>
5.1	Completeness . . . . .	16
5.2	Photometry . . . . .	16
<b>6</b>	<b>Future work</b>	<b>23</b>
6.1	LSST Processing of StarFast Simulated Sky . . . . .	23
6.2	Other LSST-DECAPS tests: w-color . . . . .	28
6.3	Astrometry . . . . .	28
<b>A</b>	<b>Appendix A: TRILEGAL and DAOphot</b>	<b>28</b>
A.1	DAOStarFinder source detection . . . . .	34
A.2	TRILEGAL queries . . . . .	34
A.3	Comparison of MAF, DAOStarFinder, and TRILEGAL counts . . . . .	34

## 1 Introduction

We report on the performance of the Large Scale Synoptic Telescope (LSST) science pipelines<sup>1</sup>, also known as 'the LSST stack', in stellar fields of varying levels of crowdedness.

The LSST will sample every night over 1,000 regions in the sky , delivering terabytes of raw data in need of processing: photometric and astrometric calibration, to deliver a calibrated exposure image, as well as a source catalog, among other image products<sup>2</sup> [7].

The survey sky is composed of regions very diverse in terms of stellar density, or crowdedness: from high density low-galactic latitude regions that have tens of millions of sources per square degree, to low-density regions towards the galactic poles with less than thousand sources per square degree.

Deblending and successful photometry is an inherent part of any astronomical data processing pipeline. There exists a body of research answering questions that are specific to crowded stellar fields, eg. how many beams do we need per source (see [2]), or how the crowded fields photometry can be approached in the era of large telescopes [8] Other studies involved eg. HyperSuprime CAM pipeline ( developed in parallel with the LSST Stack), recognizing that the deeper the survey, the higher the stellar densities encountered, and the onset of blurring the boundaries between deblending, measurement, and detection [1].

In this report we compare the 'out-of-the-box' LSST Stack tools, in particular processCcd.py, to the DECAm [Galactic] Plane Survey (DECAPS) catalogs based on the NOAO state-of-the-art community pipeline ( [9]). First we use the LSST Metrics Analysis Framework Galfast simulation of the night sky find regions representing various stellar densities - see Sec. 2. Then we query the DECAPS image database for images that were taken at exposures and filters that reach similar depth to the LSST single-visit depth (Sec. 3). We select few DECAPS exposures at each density level, and process with LSST Stack tools (Sec. 4). In Sec. 5 we compare the results of LSST processing and the DECAPS single-epoch catalogs, and develop the quality metrics. Finally in Sec. 6 we make recommendations for future work.

<sup>1</sup><https://pipelines.lsst.io>

<sup>2</sup><http://ls.st/LSE-163>

## 2 Identifying density regions

To identify regions representing different stellar densities we use the LSST Metrics Analysis Framework<sup>3</sup> simulated stellar density map prepared by P. Yoachim and L. Jones<sup>4</sup>

The resulting dataset starDensity\_r\_nside\_64.npz contains 64 magnitude bins, with the entire sky divided into 49152 healpixels<sup>5</sup>. Each healpixel contains information about the number of stars per square degree in a given magnitude bin in the simulated sky - see Fig. 1.

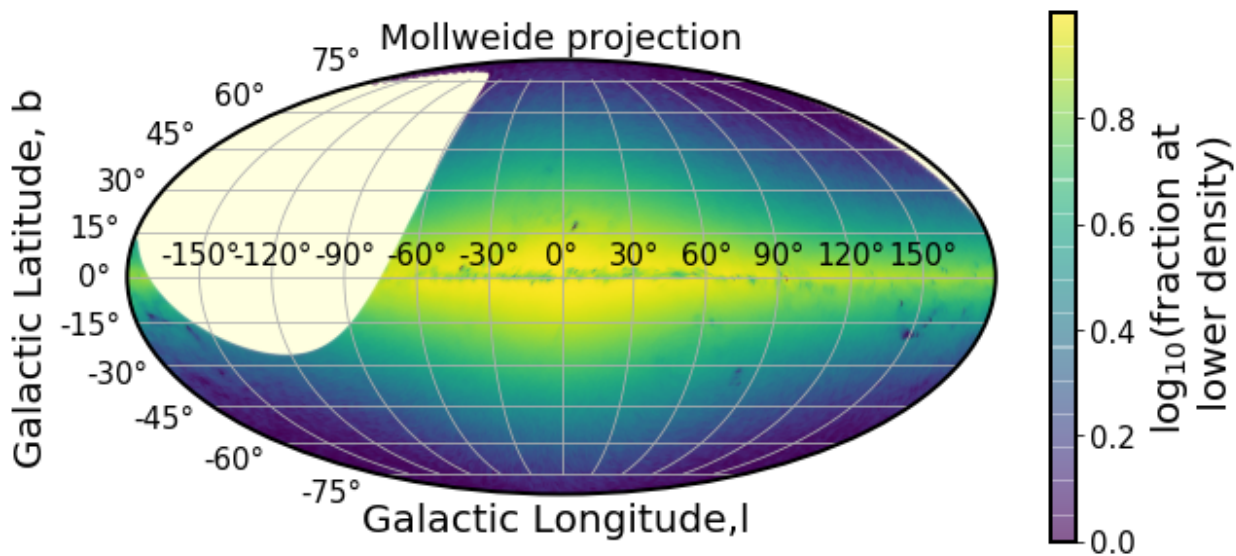


FIGURE 1: MAF healpixels plotted in galactic coordinates in Mollweide projection. The brightest regions correspond to highest stellar densities. The missing part in the higher declination is the part of the sky above  $\delta > 40^\circ$ , which is not observable from the southern location of Cerro Pachón.

To match the LSST single-visit depth, we select magnitude bins smaller than  $r=24.5$ . For each healpixel we calculate the number of pixels that have a higher stellar count. Since each healpixel has an equal area, the fraction of pixel number above a certain threshold corresponds to the fraction of sky area above given density limit. Fig. 3 illustrates how we define percentiles of stellar densities, so that eg. 'top 1%' density means that only 1 in 100 pixels has a higher density than a given pixel, and 'top 10%' means that '10 %' of pixels in the considered simulation of the sky.

<sup>3</sup><https://www.lsst.org/scientists/simulations/maf>, and [https://github.com/lsst/sims\\_maf](https://github.com/lsst/sims_maf)

<sup>4</sup>[sims\\_maf/python/lsst/sims/maf/maps/createStarDensitymap.py](https://github.com/lsst/sims_maf/blob/python/lsst/sims/maf/maps/createStarDensitymap.py)

<sup>5</sup><http://healpix.sourceforge.net>

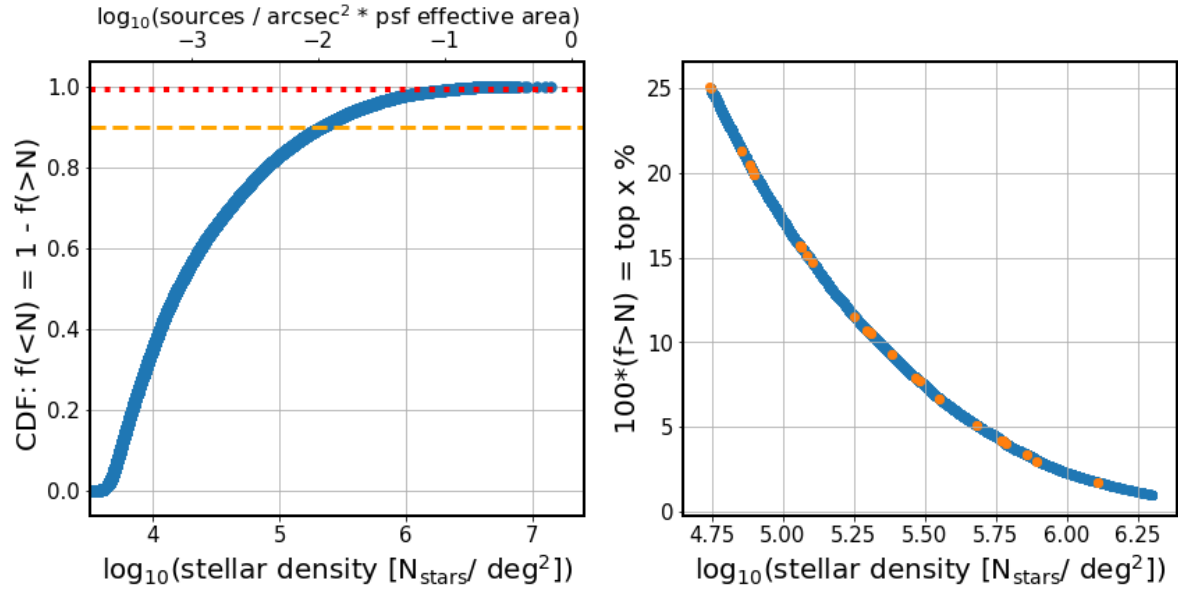


FIGURE 2: Using the Galfast sky simulation to choose DECAPS fields sampling different density regions. The left panel shows the stellar density as a function of the fraction of the sky at smaller density. It is equivalent to the cumulative distribution function. Given the stellar density per simulated healpixel, we count the number of healpixels at greater density. Normalized to the number of pixels, given their equal area, it corresponds to the fraction of the sky at greater stellar density. Horizontal dashed lines illustrate selecting pixels at top 1% or 10% density. The right panel focuses on the 1-CDF, converted to %, between 1 and 25%. It implies that according to the simulation, the density of 200 000 stars per sq.deg. corresponds to 5% of the sky, and only 1% of the sky has more than  $10^6$  stars per sq.deg. The upper axis represents the dimensionless density parameter  $N_{\text{beam}} = \text{N}_{\text{stars}}/\text{arcsec}^2 * A_{\text{PSF}}$ , with the PSF effective area  $A_{\text{PSF}} = 0.64 \text{arcsec}$ .

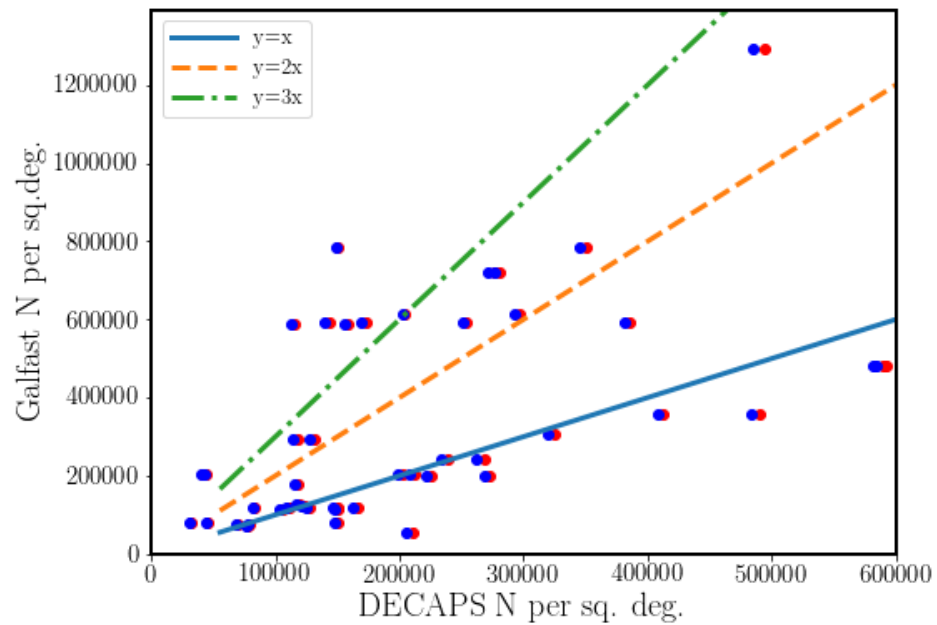


FIGURE 3: Comparison of DECAPS counts in the cleaned catalog (red dots) and raw single-epoch catalog (blue dots), vs. Galfast simulated stellar count in that region of the sky. Overplotted are the line of equivalence  $y=x$ , and its multipicities ( $2x, 3x$ ). It shows that the simulation may be not more accurate than up to a factor of a few, but it is nevertheless useful for defining density regions.

Since this definition of density includes all pixels that are within 'top 20%', we take selection around the percentiles so that :

- top 1 % means fraction of sky with greater density is 0.01
- 5 % region means such that between 4% and 6%
- 20 % region includes 19% - 21%
- 50 % region includes 49% - 51%

We illustrate the location of pixels representative of these density brackets on the sky in Fig. 4.

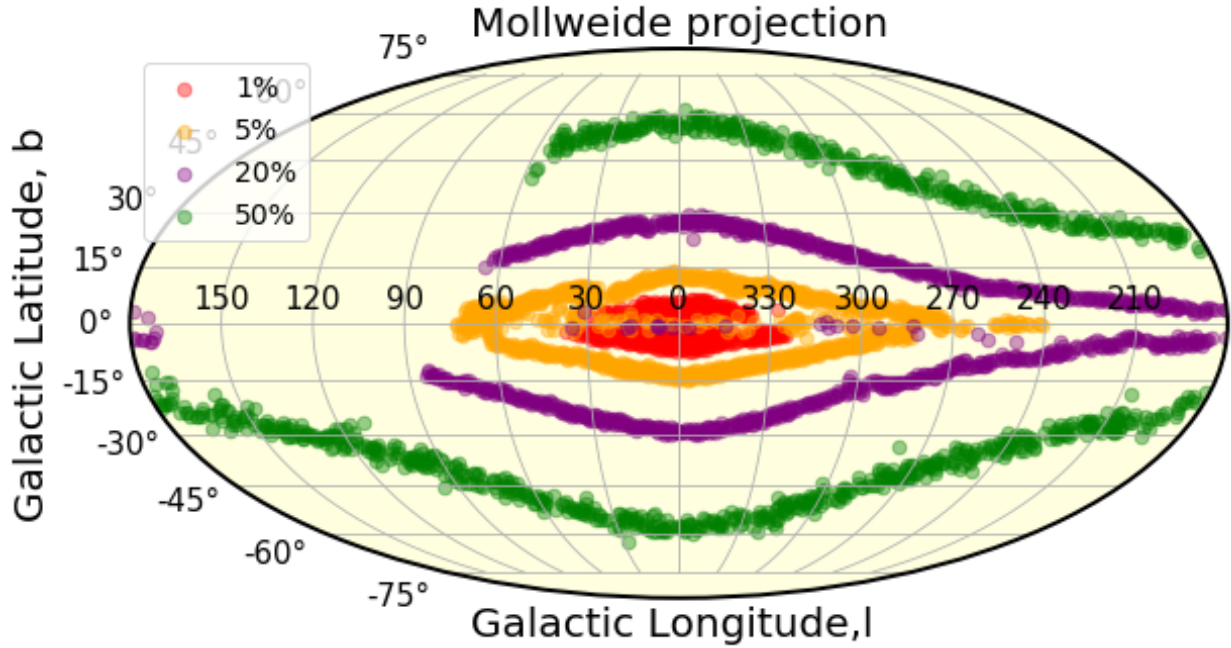


FIGURE 4: Illustration of location of regions representative of different relative density in cylindrical projection, galactic coordinates. The highest density regions are located close to the galactic bulge, and the decreasing density regions approximately trace isophotes of the Milky Way. The 20% regions close to the galactic equator correspond to high extinction regions that appear to have less counts due to interstellar dust.

### 3 DECam Plane Survey

To analyze the performance of the LSST Stack with real data, we used the Dark Energy Camera (DECam) imaging, taken as part of the DECam Plane Survey (DECAPS) [9], at the 4-m Cerro

Tololo Inter-American Observatory telescope (CTIO)<sup>6</sup>. On Fig. 5 we overlay the locations of all DECAPS fields on top the MAF map of the LSST sky. All DECAPS single-epoch images were processed with the DECAPS pipeline, resulting in single-epoch catalogs. The headers of all catalogs were assembled into the image database that contains information about single-visit exposure time, filter, time of observation, position, etc. It was used to select DECAPS fields with single-epoch depth similar to that of the single-visit depth of 30 sec LSST exposure. Thus we selected DECAPS fields with exposure between 90 and 125 sec, taken in u, g, r, or VR filter.

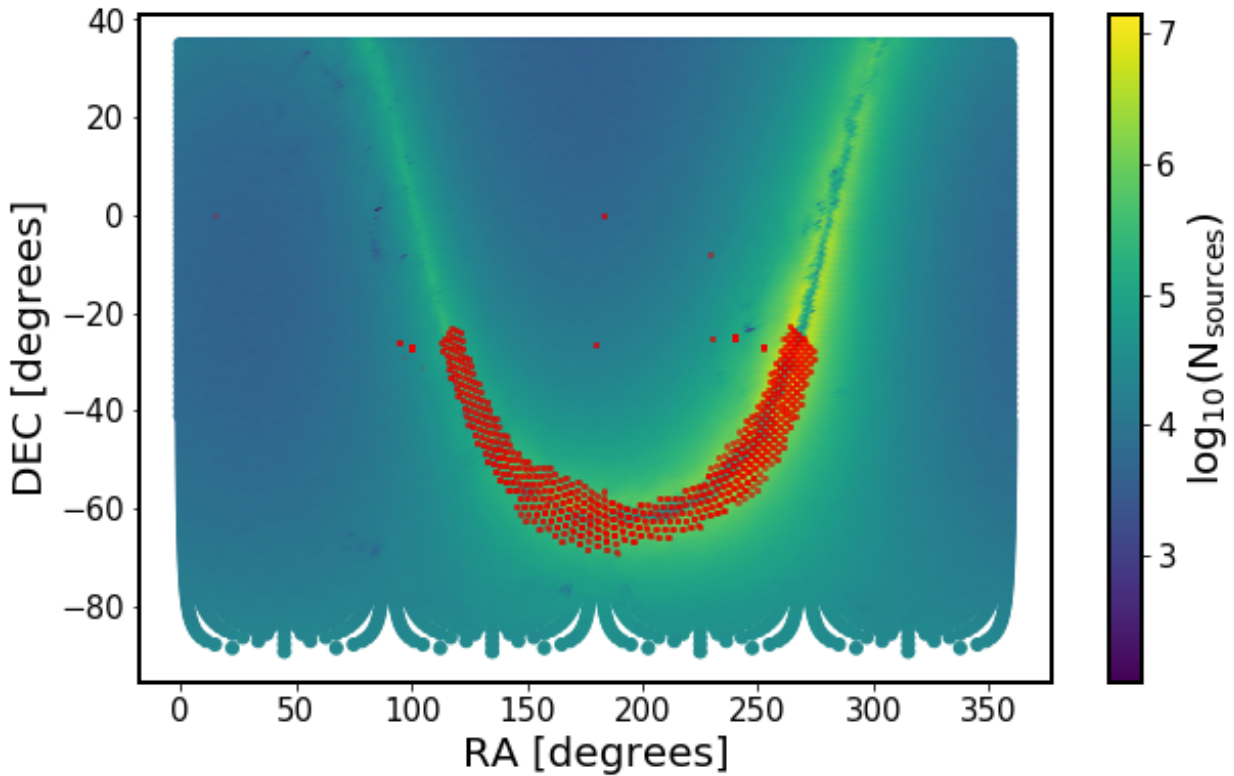


FIGURE 5: All DECAPS fields, overlaid on the map of healpixel stellar densities from MAF simulated sky. We matched the position of the center of each DECAPS field to the nearest healpixel to obtain an estimate of stellar density at each DECAPS field. In this way we selected DECAPS fields representative of various stellar densities (eg. 5%, 10%, 15%, as explained in Sec. 2).

We cross-matched the DECAPS image database with the stellar density information contained in MAF healpixels. Each DECAPS image plane is tiled by a mosaic of 62 CCDs (see Fig. 6). The size of each CCD element of the DECam image plane mosaic is 2046x4094 pixels, with pixel scale of 0.27 arcsec / px, so that a single mosaic element covers an area of 0.047117 square °. A single DECam exposure is also called a visit, and with 62 mosaic elements the full field of

<sup>6</sup>see <http://www.ctio.noao.edu/noao/node/1033>

view  $2.2^\circ$  wide is several times bigger than the full moon. This makes it comparable to the LSST  $3.5^\circ$  wide field of view. Using the coordinates of the center of each DECAPS field we found the nearest healpixel within  $0.5^\circ$ .

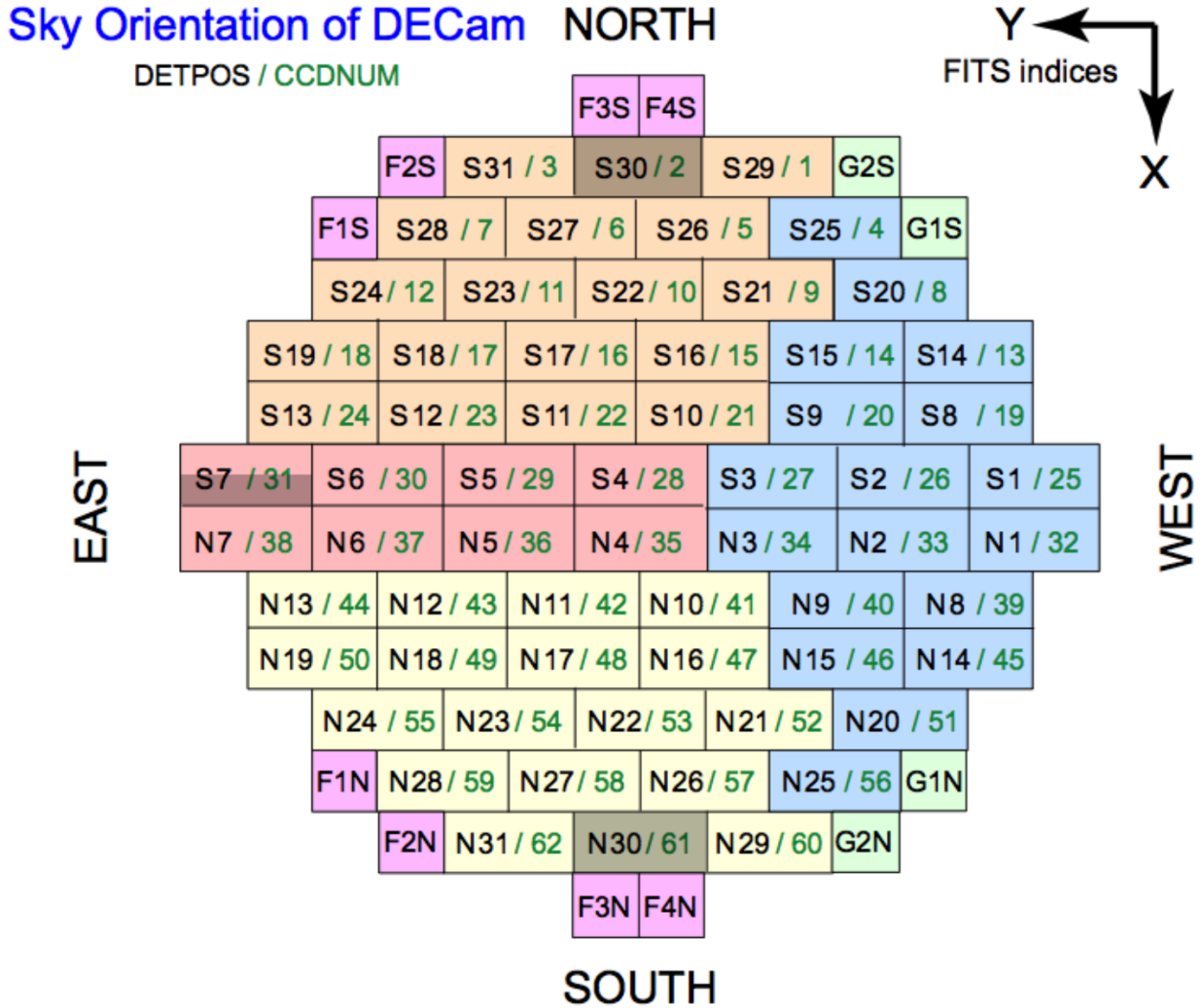


FIGURE 6: An illustration of the DECam CCD mosaic image plane, adapted from Fig.4-3 in NOAO Data Handbook [10]. The color corresponds to the one of the four sets of read-out electronics (orange,pink,blue,yellow), or the guiding (green) and focus (magenta) CCDS. The grey CCDs do not function properly. For this reason S30, S7, and N30 were excluded from the analysis.

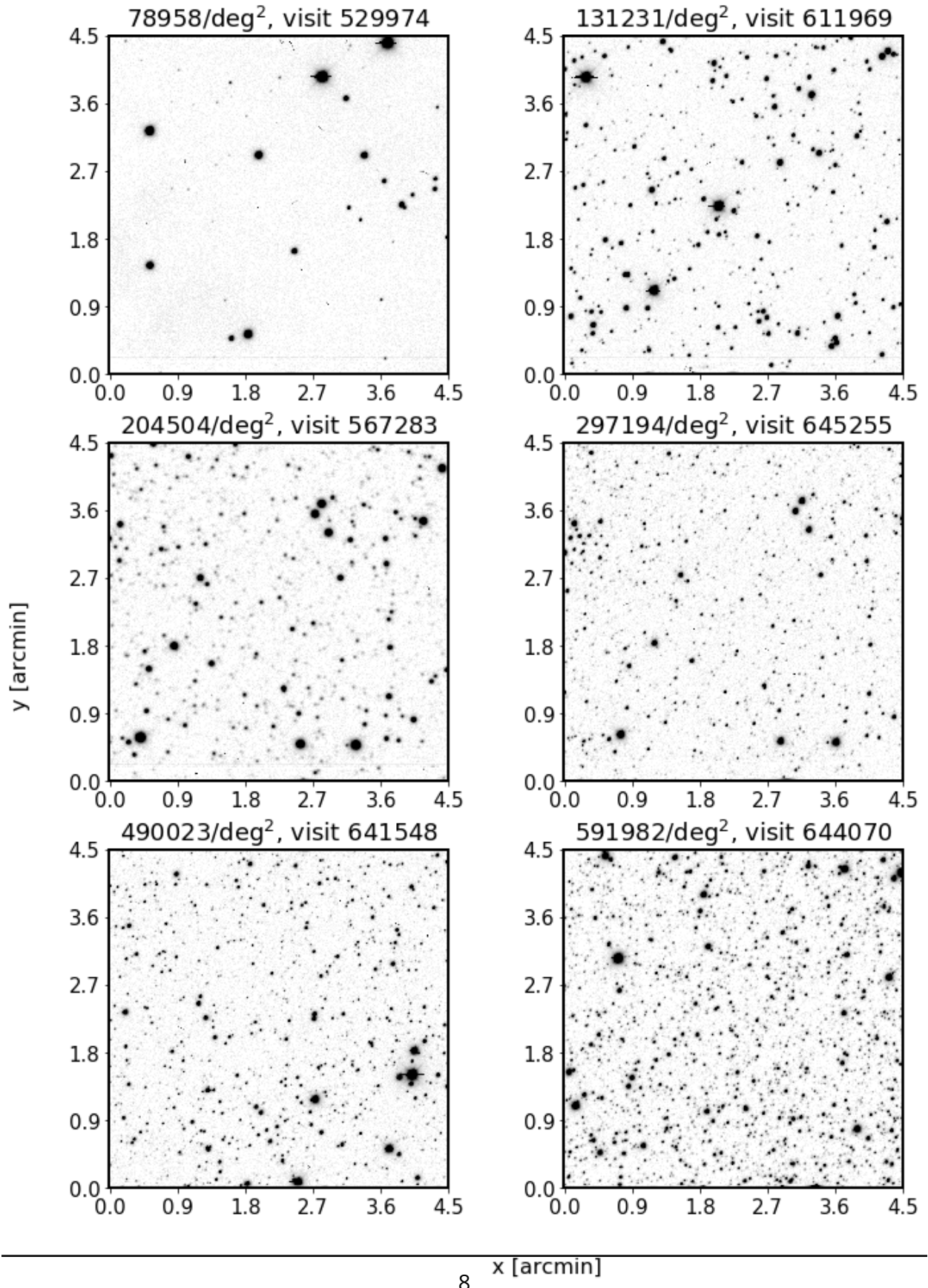


FIGURE 7: Illustration of regions of different stellar count in the cleaned DECAPS single-epoch catalogs. As shown on Fig. ??, the Galfast count (and therefore % level), does not always cor-

TABLE 2: LSST pixel mask bit values.

Bit position	Description	Mask decimal value
0	bad	1
1	saturated	2
2	interpolated	4
3	cosmic ray	8
4	edge	16
5	detected	32
6	detected negative	64
7	suspect	128
8	no data	256

## 4 LSST Processing of DECAPS data

The DECAPS calibrated imaging was processed with the LSST Science Pipelines installed on the LSST-dev machine installed at the NCSA. We specifically employed processCcd.py and the standard Stack configuration. Transferring the resulting source catalogs and calexp files over scp we analyzed the output on a laptop using jupyter notebooks.

To obtain independent order of magnitude comparison to MAF simulation, and LSST/DECAPS processing of DECam data, we also queried TRILEGAL simulation data, and processed the DECam images with DAOPhot - see Appendix A.

The big picture is to find how metrics that we develop behave as a function of source crowdedness. We consider completeness, and photometric accuracy.

### 4.1 Cleaning DECAPS catalog, comparison to LSST pixel mask

To compare LSST and DECAPS catalogs, we cleaned both catalogs with the flags assigned to each source by the respective image processing pipeline. To verify the validity of DECAPS source flags, we compared them with the LSST pixel-level mask information stored in the FITS Header Data Unit. Pixel-level masks are encoded in 8 bits, each of which can be 'on' or 'off', signifying that a given flag was 'on' or 'off' for a given pixel. The total value of the mask at each pixel is a decimal representation of such eight bits binary number, eg.  $(00100001)_2 = 2^0 + 2^5 = 1 + 32 = (33)_{10}$  means that bit '0' and '5' are 'on' (counting from the right). See Table 2 for details.

TABLE 3: DECAPS flags. We excluded sources with flag bits 1,3,4,5,6,8,20,22.

Bit position	Description
1	Bad pixel
3	Saturated
4	Bleed trail
5	Cosmic ray
6	Low weight
8	Long streak
20	Additional bad pixel
21	Nebulosity
22	S7 amplifier B

For each visit we considered DECAPS single-epoch source catalog, and the LSST calexp image. For each DECAPS source, given the pixel coordinates, we retrieved the value of the LSST mask at that pixel. Given the understanding of the LSST flag bits (Table 2) we performed a bitwise and with a mask filter  $(1101111)_2 = (2^1 + 2^2 + 2^3 + 2^4 + 2^6 + 2^7)_{10}$ , flagging a source as 'lsst bad' if either of the flag bits apart from '5' (detected) was 'on'.

Each DECAPS source also has a flag where the value is composed of bits inherited from the NOAO Community Pipeline and new flags(see Table 3). We performed a bitwise and with the mask filter  $(2^1 + 2^3 + 2^4 + 2^5 + 2^6 + 2^8 + 2^{20} + 2^{22})_{10}$ , flagging the source as 'decaps bad' if either of this bits were 'on'. We compared which sources would be excluded based on the DECAPS source-level flags vs LSST pixel-level masks, and we found that for a particular visit 611980 the overlap between sources excluded based on LSST pixel mask vs DECAPS source flags is 99%. This means that DECAPS flagging is consistent with the LSST mask information, and the same sources would be 'excluded' based on either DECAPS flags or LSST mask information. For this reason we cleaned the DECAPS catalog with source level flags.

## 4.2 Cleaning LSST catalog

The LSST source catalog contains per source a list of 83 flags that could be set 'on' or 'off'. Of these, flags number 60:72 are base\_PixelFlags\_flag, meaning they contain information relevant to the level of source detection, rather than processing. See Table 4 for detailed description.

We clean the LSST source catalog from sources that have flags number 62 (edge) or 67 (inter-

TABLE 4: LSST source flags explanation. All flags names start with 'base\_PixelFlags\_flag' which was omitted in the flag\_name column below.

number	name	explanation
60	flag	general failure flag, set if anything went wrong
61	offimage	Source center is off image
62	edge	Source is outside usable exposure region (masked EDGE or NO_DATA)
63	interpolated	Interpolated pixel in the Source footprint
64	saturated	Saturated pixel in the Source footprint
65	cr	Cosmic ray in the Source footprint
66	bad	Bad pixel in the Source footprint
67	suspect	Source's footprint includes suspect pixels
68	interpolatedCenter	Interpolated pixel in the Source center
69	saturatedCenter	Saturated pixel in the Source center
70	crCenter	Cosmic ray in the Source center
71	suspectCenter	Source's center is close to suspect pixels
72	flag	General Failure Flag

polatedCenter)<sup>7</sup>. Other flags would remove too many sources that have only small 'defects', eg. 64 (interpolated) is on for a bright source on the footprint of which there is a cosmic ray, and 65 (bad) is on for any source which has even one bad pixel in the footprint -see Fig. ???. A comparison of the starting source count and final source count (after cleaning ) is shown on Fig. 9, and Table 5

Given the single-epoch DECAPS source catalogs, and the LSST source catalogs, we followed a uniform set of procedures to clean both datasets, and in turn cross-match positionally. First we made a quality cut removing all sources with signal-to-noise ratio smaller than five:  $S/N < 5$ . The number of sources thus removed depends on a visit number, but does not exceed few % of the catalog. Following that we also removed sources with flags that correspond to bad, edge detections, cosmic rays, or saturation spikes (as outlined in Sec. 4.1 and 4.2). The LSST Processing Pipeline deblends sources in a similar fashion to the SDSS Imaging Pipeline<sup>8</sup>. For the LSST source catalog, we chose to keep only those sources that were either isolated parents ( parentId=0, nchild=0), or deblended children (parentId != 0 , nchild=0) (see Table 7 for details.)

<sup>7</sup>This is similar to the example in Sec.4 of SDSS Image Processing I: The Deblender [3]

<sup>8</sup>SDSS Image Processing I: The Deblender [3], SDSS Image Processing II: The Photo Pipelines [4], [6], and [5]

TABLE 5: A summary of all LSST-processed DECAPS visits. The column ‘visit’ corresponds to the DECAPS visit number. The following four columns (‘N raw’, ‘N f’, ‘-N r’, ‘=N c’) contain the source counts per visit area ( $\approx 2.74 \text{ deg}^2$ ). ‘N raw’ is the input number of sources per visit , summing over all CCD source catalogs. ‘(N f)’ is the number of sources removed due to bad flags. ‘-N r’ is the total number of removed sources ( due to flags, low S/N, or sources that in the LSST deblending process are neither isolated parents, nor deblended children). ‘=N c’ is the final number of clean sources per visit (‘N raw’ - ‘N r’= ‘N c’). ‘N c/deg<sup>2</sup>’ is ‘=N c’ converted to count per deg<sup>2</sup>. N MAF/deg<sup>2</sup> is the predicted number of sources per deg<sup>2</sup> at that location based on Galfast simulation.  $\rho_{MAF}$  is the MAF density; eg. 21.3 is the top 21.3% stellar density of the simulated sky.

Visit	$N_{\text{raw}}$	( $N_f$ )	$-N_r$	= $N_c$	$N_c/\text{deg}^2$	$N_{MAF}/\text{deg}^2$	$\rho_{MAF}$	$N_{loSN}$	$N_{\text{parents}}$	$N_{\text{blend}}$
568172	29809	9148	12434	17375	6241	72072	21.3	12986	153919	7772
527319	120862	13744	39638	81224	29175	79632	19.9	34282	112848	2821
530012	160406	15210	61337	99069	35585	203040	10.6	51669	20425	214
525846	167582	15247	63295	104287	37459	203040	10.6	51949	96932	3172
525900	171337	15037	58219	113118	40631	79632	19.9	46796	70011	973
529989	182933	15910	61808	121125	43508	79632	19.9	49120	114760	5474
529974	228849	16842	67339	161510	58014	76572	20.5	44712	104406	2698
525814	235307	16811	72214	163093	58582	76572	20.5	50998	98063	2812
527096	227256	16100	59686	167570	60191	55908	25.0	36748	85483	1613
644125	242521	16387	72363	170158	60101	72072	21.3	40731	89237	1786
611980	273032	18816	76043	196989	70758	116856	15.6	41383	78662	4251
527247	264383	15283	66539	197844	71065	116676	15.6	38391	138758	5972
567283	280305	16981	68379	211926	76123	612648	4.0	30908	230049	6459
527555	313294	1173	81585	231709	83229	783324	3.0	39458	127709	4957
612757	317270	4014	84877	232393	82084	292788	7.9	42468	128543	5064
527246	319929	18136	86268	233661	83930	114588	15.7	47233	128325	5865
640891	355861	24520	107462	248399	87737	121536	15.1	60163	127665	4569
611970	377917	26716	120640	257277	92413	178992	11.5	80884	133384	5352
645251	348033	18786	89669	258364	91257	128016	14.7	41210	129397	3413
527296	361951	21167	101452	260499	93571	588096	4.2	63149	144777	5063
611969	387056	25752	118639	268417	96415	292788	7.9	74291	162439	7030
526413	368017	22267	98745	269272	96722	78480	20.1	52626	151602	8267
525838	371329	19984	100644	270685	97229	116676	15.6	54839	71782	1611
525837	393879	22350	107414	286465	102898	114588	15.7	56743	74171	1458
611529	398924	22625	105677	293247	105334	116856	15.6	54741	113152	8653
527552	395446	1716	99214	296232	106406	591336	4.2	44093	95415	7272
525920	415231	22439	111423	303808	109127	588096	4.2	59375	133660	5528
527300	436689	24839	120330	316359	113635	594324	4.2	70470	170980	8268
644035	435830	2170	106363	329467	116371	205308	10.5	46535	93985	4830
525904	479294	26679	135534	343760	123478	594324	4.2	77080	112960	6774
527453	495629	28732	139172	356457	128039	242316	9.3	80487	208259	1378
609754	490143	26233	121738	368405	132330	116856	15.6	62319	199832	1515
530032	486203	23112	115217	370986	133257	198432	10.7	51002	176645	1130
526152	520842	28739	143336	377506	135599	55404	25.1	77724	142876	1000
567795	508405	26663	129592	378813	136069	721728	3.4	63447	62120	4248
641497	529827	28546	137626	392201	138530	205308	10.5	59868	184493	1396
640995	571174	2973	155705	415469	146748	242316	9.3	85262	171899	6766
527064	558264	26197	132299	425965	153006	591336	4.2	56098	184352	5900
566793	560376	1088	134186	426190	158458	1292976	1.7	59842	132416	6062
644205	571378	4663	142463	428915	151498	721728	3.4	65955	165636	4585

TABLE 6: A summary of all single-epoch DECAPS source catalogs, with columns as in Table 5. See Fig. 9 comparing the 'N raw' converted to number of sources per square degree, and 'N clean per sq.deg.'

Visit	$N_{raw}$	$(N_f)$	$-N_r$	$= N_c$	$N_c/\text{deg}^2$	$N_{MAF}/\text{deg}^2$	$\rho_{MAF}$
568172	16824	138	150	16674	5989	72072	21.3
527319	92326	2819	3039	89287	32071	79632	19.9
530012	121313	3293	3982	117331	42145	203040	10.6
525846	125245	3135	3457	121788	43746	203040	10.6
525900	127722	2557	2786	124936	44876	79632	19.9
529989	140043	2527	2803	137240	49296	79632	19.9
527096	194837	2126	2290	192547	69162	55908	25.0
525814	200562	4481	4938	195624	70268	76572	20.5
529974	224231	3992	4413	219818	78958	76572	20.5
644125	228088	5570	6182	221906	78380	72072	21.3
527247	237656	4858	5144	232512	83518	116676	15.6
527246	301083	5469	5907	295176	106027	114588	15.7
611980	315722	6779	7397	308325	110750	116856	15.6
527296	330295	7176	7726	322569	115866	588096	4.2
611970	340528	9668	10513	330015	118541	178992	11.5
612757	342629	8541	9473	333156	117674	292788	7.9
645251	343358	5546	6253	337105	119069	128016	14.7
640891	361837	9423	10389	351448	124135	121536	15.1
525838	360793	6057	6515	354278	127256	116676	15.6
611969	376588	10280	11243	365345	131231	292788	7.9
527300	409385	8974	9654	399731	143583	594324	4.2
611529	428299	9981	11167	417132	149833	116856	15.6
527555	421706	3848	4285	417421	149937	783324	3.0
525837	425261	6791	7437	417824	150082	114588	15.7
526413	428035	8417	9137	418898	150467	78480	20.1
525920	449868	6675	7430	442438	158923	588096	4.2
609754	474355	10034	11677	462678	166193	116856	15.6
525904	490306	8413	9118	481188	172842	594324	4.2
567283	575760	5549	6426	569334	204504	612648	4.0
644035	583432	9457	10948	572484	202208	205308	10.5
526152	599164	12579	14023	585141	210182	55404	25.1
641497	611424	10156	11324	600100	211962	205308	10.5
530032	638179	9776	10964	627215	225295	198432	10.7
527453	682113	14654	16569	665544	239062	242316	9.3
527552	714305	6031	6893	707412	254101	591336	4.2
525879	772457	11625	13117	759340	272754	198432	10.7
640995	783011	17946	20850	762161	269204	242316	9.3
567795	791019	9439	11056	779963	280162	721728	3.4
644205	800175	13601	15899	784276	277016	721728	3.4
645255	852539	9620	11135	841404	297194	612648	4.0
641500	935661	14131	16133	919528	324788	305280	7.7
644082	1007998	12826	15633	992365	350515	783324	3.0
526028	1035808	17929	20772	1015036	364600	305280	7.7
527064	1085375	10200	12399	1072976	385412	591336	4.2
644011	1181972	11059	13806	1168166	412611	355896	6.7
566793	1350724	12414	22431	1328293	493863	1292976	1.7

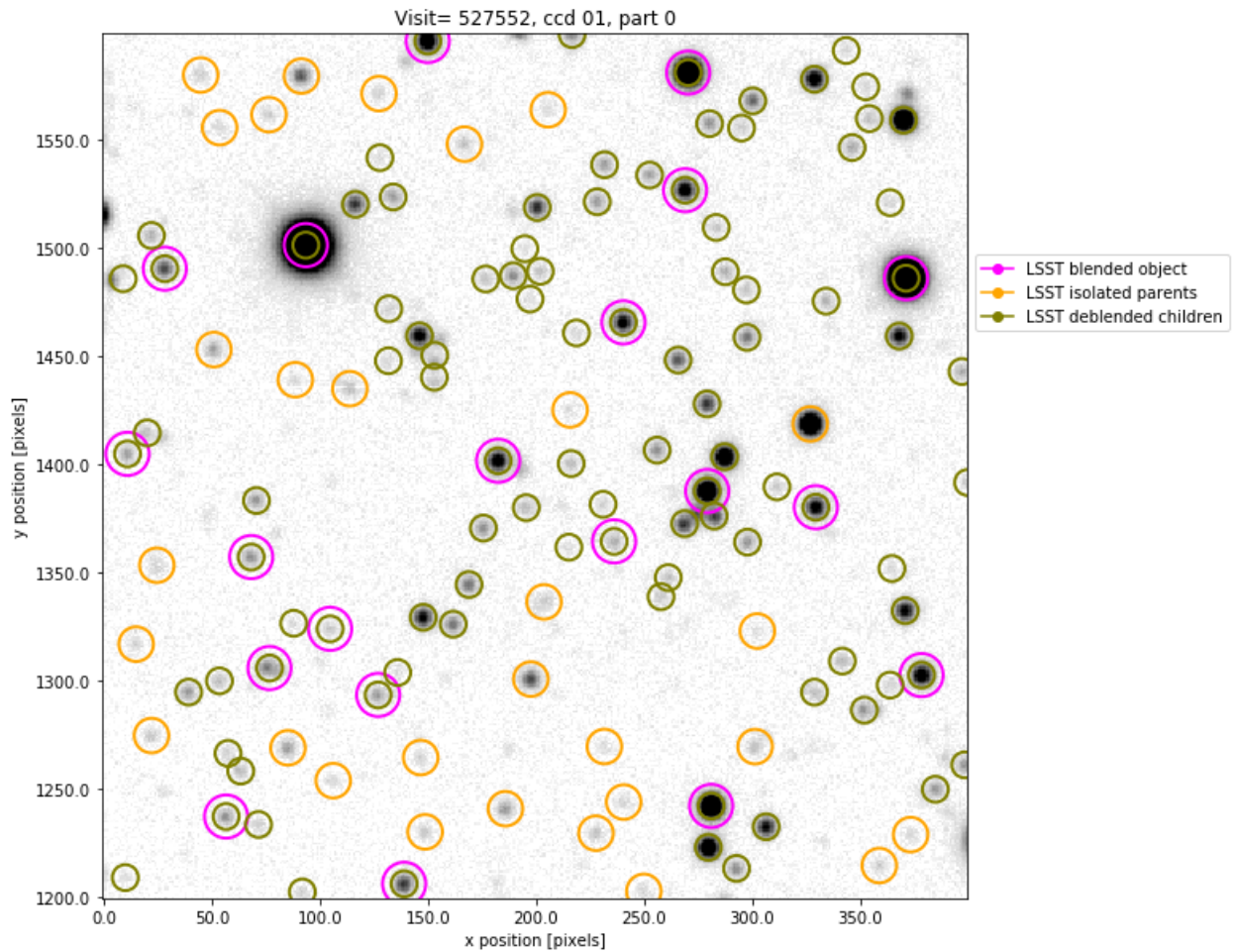


FIGURE 8: We illustrate the sources as reported by the LSST pipeline for a small region of CCD01 of visit 527552. A source may be reported as an isolated source (yellow), or a blend (magenta). If it is a blend, it may become successfully deblended producing deblended children (green). In what follows, we remove blended sources, and only keep isolated parents and deblended children.

TABLE 7: Summary of possible parentId and nchild combinations for blended sources in the LSST Science Pipeline. An example count in the final column is provided for visit 525814, a top 20% density region, which has the raw source count 235307. For that visit 16811 sources had bad flags, 49901 had  $S/N < 5$ , and in total 163093 were kept in the clean catalog.

parentId	nchild	type	decision	count
0	0	parent: isolated source	keep	104406
0	>0	blended source	remove	26981
!=0	0	deblended child	keep	103920
!=0	>0	failure case	remove	0

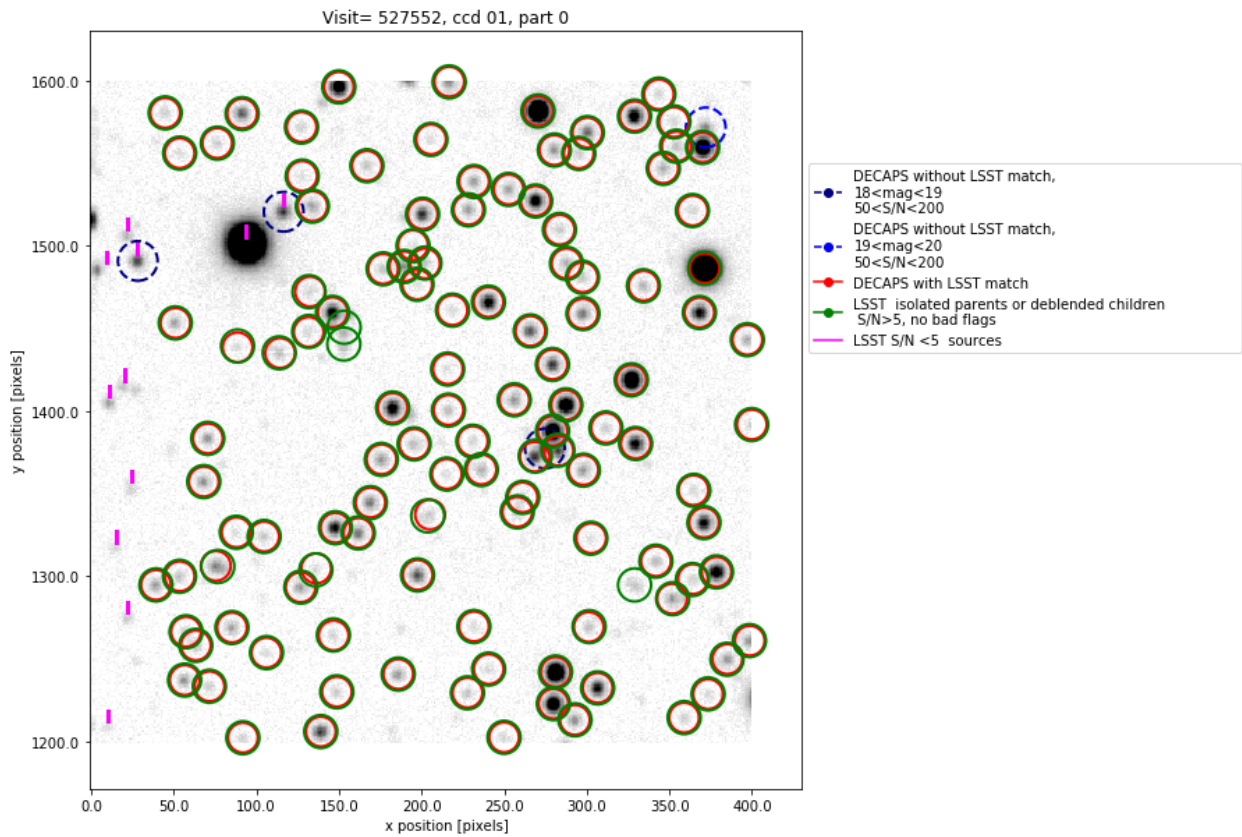


FIGURE 9: The same region as on Fig. 7. Green circles mark the position of retained LSST sources: isolated parents, or deblended children, with  $S/N > 5$ , and no bad flags. Red circles mark the position of DECAPS detections with an LSST match. Vertical magenta dashes are above the LSST sources with  $S/N < 5$ . Blue dashed circles mark location of DECAPS source without an LSST match. Note that e.g. at  $(x,y) = 50, 1490$  an LSST source was detected, but since its  $S/N < 5$  it was not kept in the clean LSST catalog.

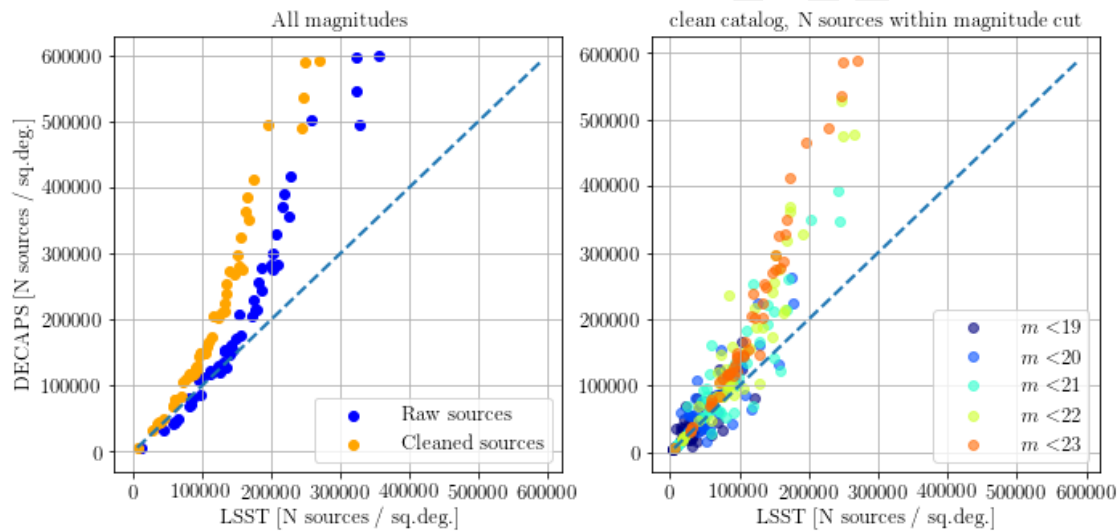


FIGURE 10: A plot of source count comparing LSST to DECAPS source catalogs of the same fields (visits). On the left panel blue dots mark raw source count, i.e. count of the input LSST source catalog or DECAPS single-epoch catalog. The source catalog count was converted to number of sources per square degree, since in some cases not all CCDs were processed. Orange dots mark the count of clean sources (see Fig. ??). As we would expect, between raw and clean catalogs the points on the diagram move vertically from top to bottom, and horizontally from right to left. For exact counts in each stellar field, see LSST counts Table 5 and DECAPS counts Table 6. The right panel shows the effect of excluding faint sources on the clean catalog: selecting only bright sources ( $m < 19$ ), DECAPS and LSST counts for all visits are closer to each other. Only adding faint sources do we reach the situation in the left panel (eg.  $m < 23$ ), where LSST significantly loses faint sources.

## 5 Metrics

Starting with cleaned LSST and DECAPS source catalogs, we consider a set of metrics to compare the quality of LSST science pipelines to the state-of-the-art DECAPS pipeline.

### 5.1 Completeness

For each visit that corresponds to a given level of crowdedness, consider the detection completeness of the LSST to the DECAPS sources. Assuming that DECAPS is the ‘true’ catalog of sources, the completeness is defined by the percentage of DECAPS sources (binned along DECAPS magnitude), that have an LSST match.

Given two catalogs, each with a set of source coordinates and photometry, one catalog is positionally cross-matched to another. This means that for each source of the first catalog is paired to the nearest source in the other catalog. The spatial separation and magnitude difference are two quantities that we choose as the basis of comparison. First, we require that to be called a ‘match’ the sources in two catalogs must have coordinates that differ by not more than  $0.5''$ . This is a very liberal cut given that the peak of the separation histogram occurs at distance smaller than  $0.3''$  for  $>98\%$  of sources in all visits (see Fig. ??). Second, we require that the sources differ by not more than 0.5 magnitudes. As illustrated on Fig. 13, this only removes the outliers. In fact, given that the majority of the sources ( $>98\%$ ) that are matched within  $0.5''$ , and do not differ by more than 0.5 magnitude, this constraint does not change the completeness by more than few %. Fig. 10) shows how completeness , and catalog counts, depend on source density ( from LSST catalog).

### 5.2 Photometry

We also considered the photometric accuracy. Since both DECAPS and LSST processing pipelines start from the same instcal calibrated DECam images, they ought arrive at similar measurement of flux, and in turn, magnitudes. The fact that there exists an offset and a spread in magnitude difference corresponds to slight differences in the details of each processing pipeline. We compare both the photometric difference between same fields processed by two different pipelines: DECAPS to LSST. Assuming that the majority of objects are non-variable in nature, we consider consecutive observations of the same stellar field at different epochs, to find the statistical variance epoch-to-epoch, thus resulting in DECAPS-DECAPS and LSST-LSST compar-

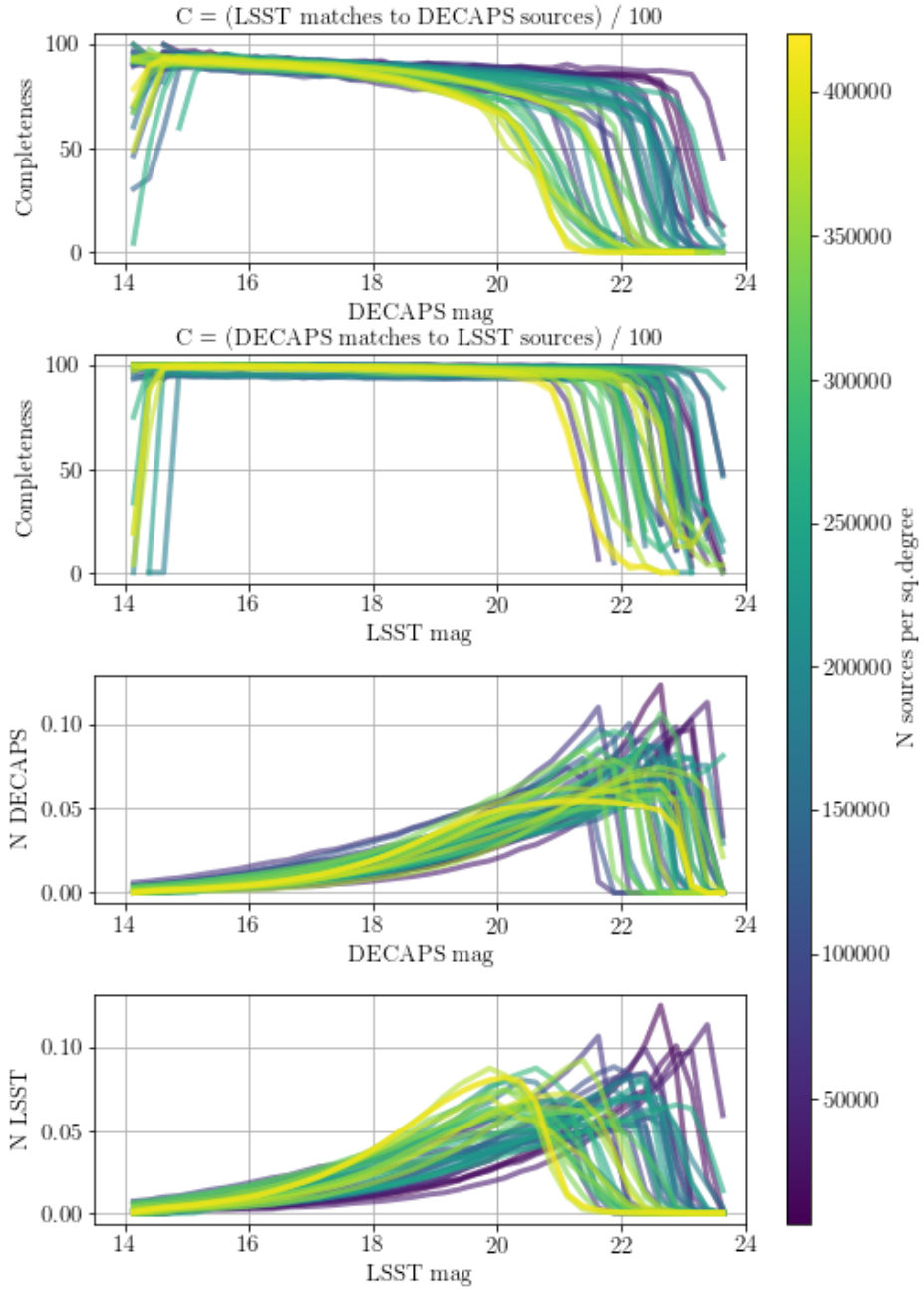


FIGURE 11: Different colors correspond to different level of stellar crowdedness, expressed in terms of number of sources per square degree (the mean between LSST and DECAPS cleaned catalogs). Top two panels show source-to-source completeness. The first of the two top panels is completeness of LSST to DECAPS, i.e. for each DECAPS source we look for an LSST equivalent. The second top panel is completeness of DECAPS to LSST , i.e. for each LSST source we find a DECAPS counterpart. The LSST-DECAPS completeness falls off quicker than DECAPS-LSST, since DECAPS catalog has more sources at fainter magnitudes (see Fig. 9). The bottom two panels show the normalized number of counts in the input catalogs. We characterize completeness by two numbers per visit: the mean completeness between 18-20 magnitude ( $C_{18-20}$ ), and the magnitude at which completeness falls to 50% level,  $m_{50}$ , plotted on Fig. 11.

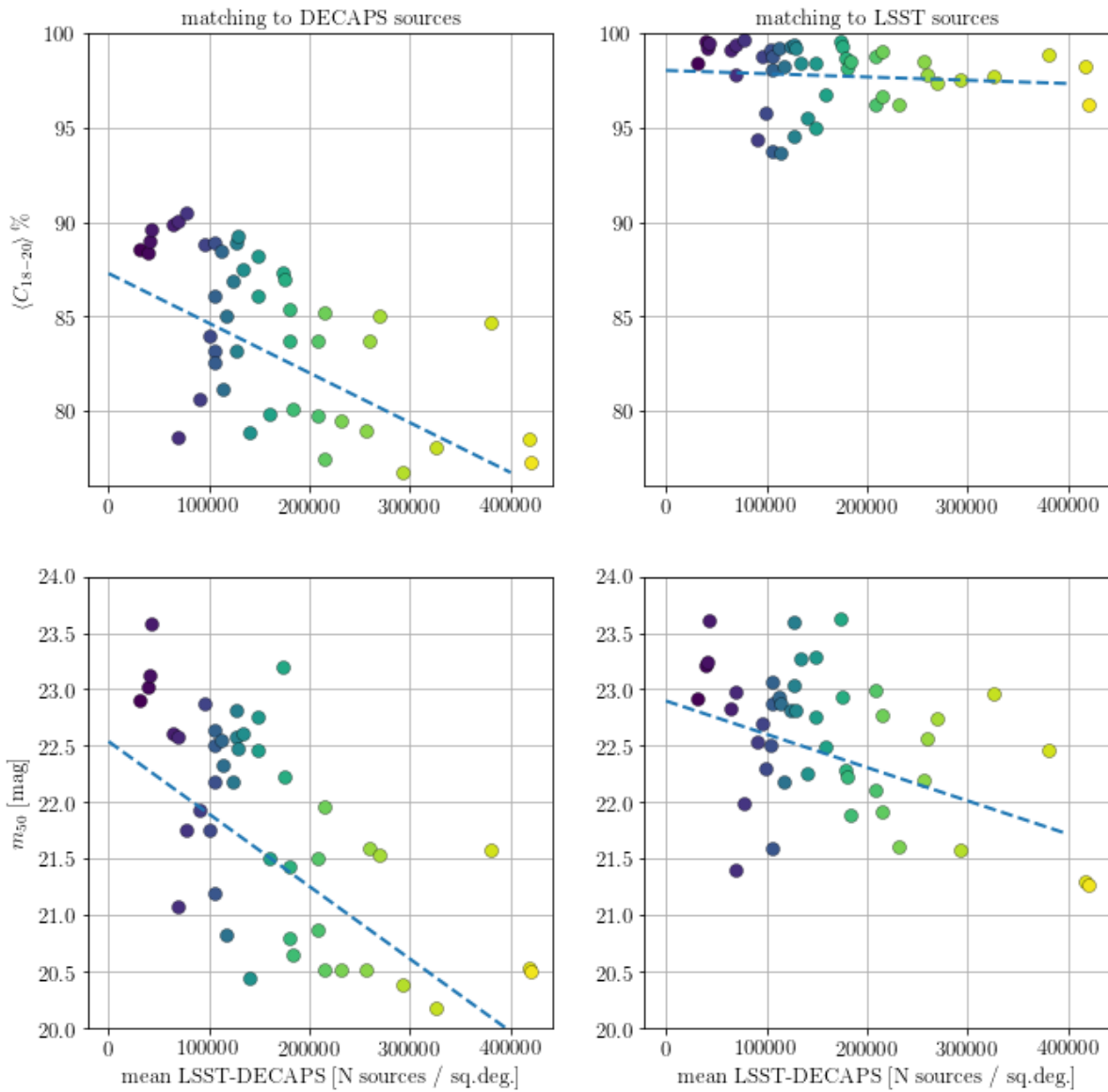


FIGURE 12: Magnitude at which completeness falls to 50% (top two panels), and the mean completeness between 18 and 20 magnitudes (bottom two panels). The panels on the left hand side correspond to the uppermost panel in Fig. 10, while the right hand side panels correspond to the second panel in that Figure. All points are colored with the same color and marker as in Fig. 10, which corresponds to the source density, hence left-to-right color gradient. In each panel we overplot the linear best-fit to show the overall trend of decreasing  $\langle C_{18-20} \rangle$  and  $m_{50}$  with source density, as expected.

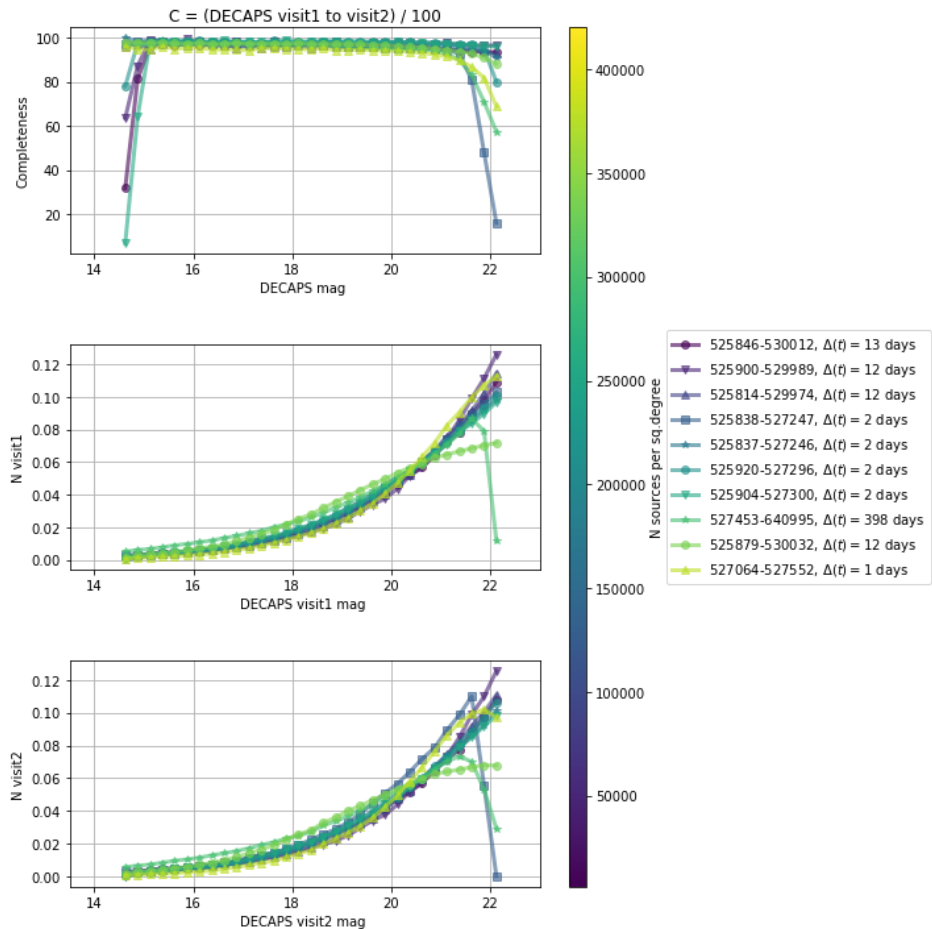


FIGURE 13: The same quantities as on Fig. 10, but corresponding to two different visits at the same location, to test the repeatability of DECAPS detections. The two visits were chosen in the same filter and at the same location, and as on completeness of DECAPS to LSST, we match source-by-source and consider the number of sources per magnitude bin in visit1 that do have a matching source in visit2.

isons.

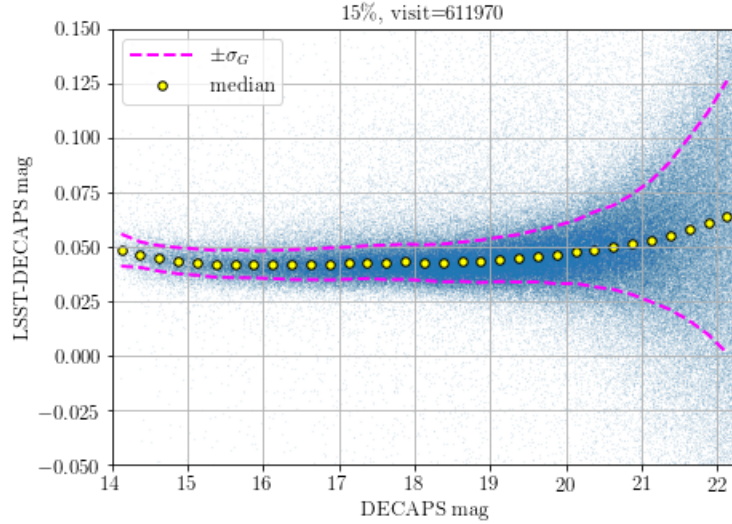


FIGURE 14: Difference in magnitudes between the DECAPS and LSST magnitudes for sources matched within 0.5 arcsec for a region in top 15% density (611970). While in calculating completeness apart from spatial proximity we require sources to be within 0.5 mag to constitute a ‘match’, here we did not exclude any outliers in calculating the median and  $\sigma_G$ , since these statistics are insensitive to outliers. We overplot the median with yellow circles, and the  $\pm\sigma_G$  envelope - the measure of scatter based on the interquartile range. The offset between LSST and DECAPS is on the level of 0.05 mag. The same quantities plotted for all fields can be shown on Fig. 15

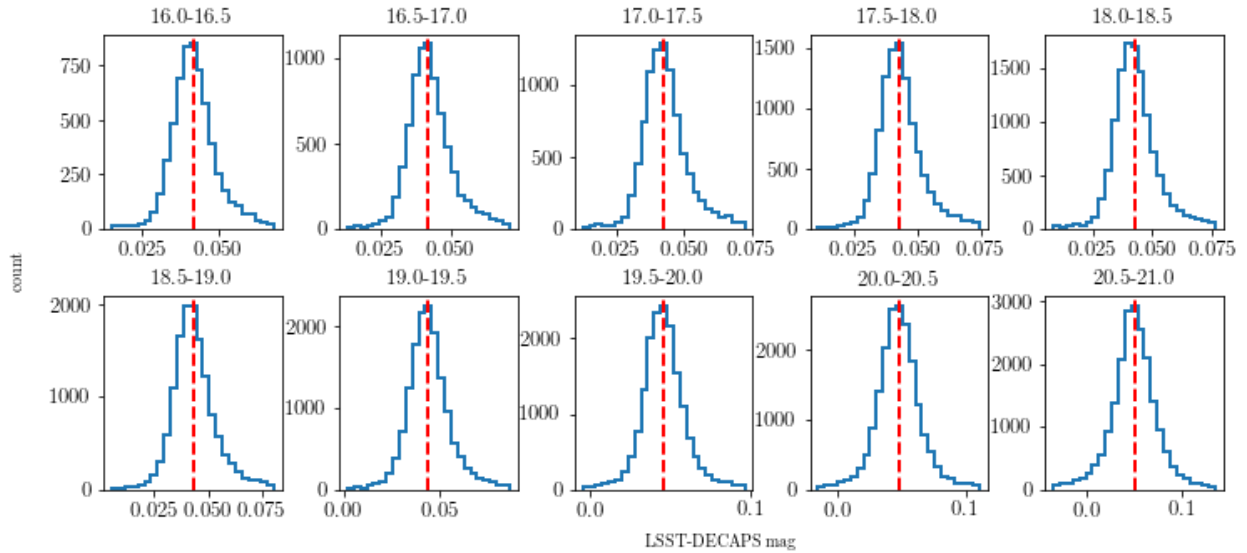


FIGURE 15: Cross-section of Fig. 15, showing the histogram of magnitude difference per DECAPS magnitude bin, plotting the median as vertical line, with each histogram limited between  $\pm 4\sigma_G$ .

For two fields per stellar density regime (5%, 10%, 15%, 20%) we found visits at exactly the

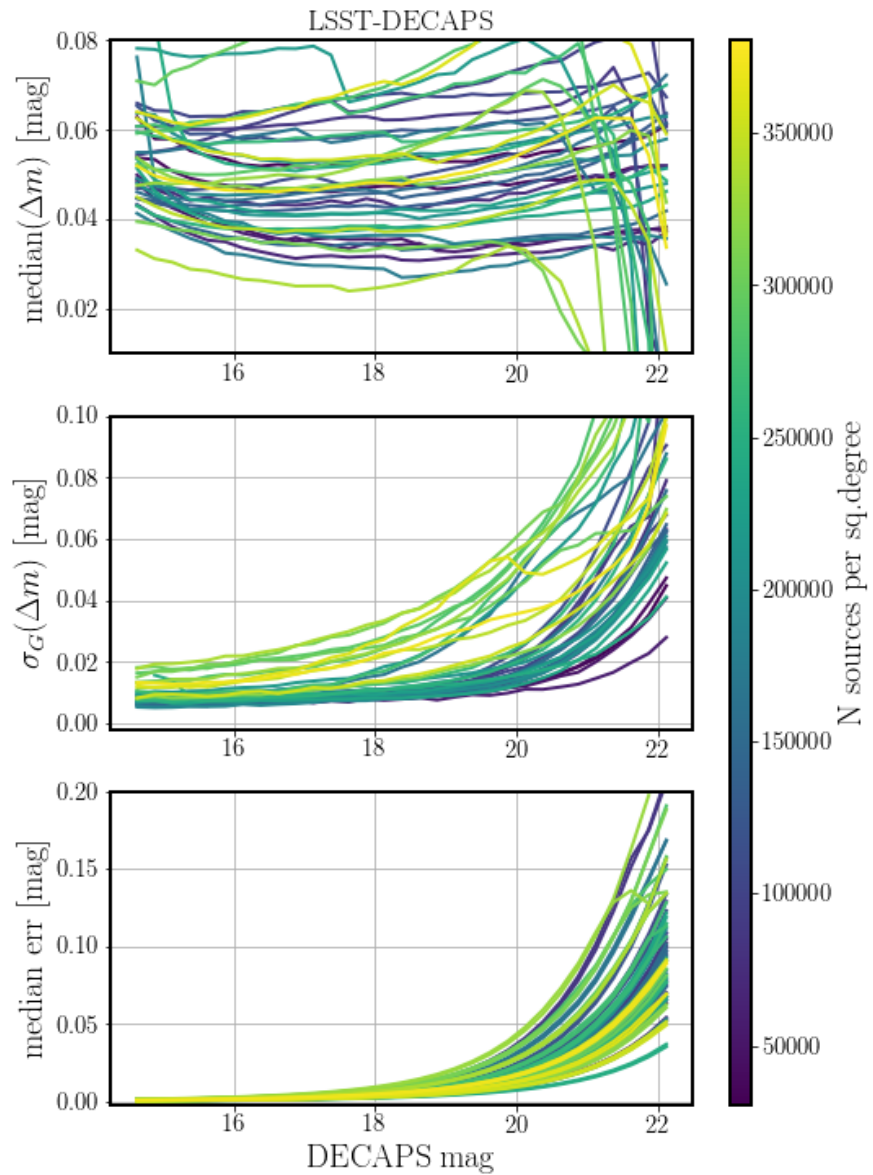


FIGURE 16: The measurement of photometric offset between DECAPS and LSST pipelines. For each visit we cross-matched source catalogs corresponding to LSST and DECAPS processing;  $\Delta m$  is the difference in magnitude reported between DECAPS and LSST for the same source. For each visit we bin sources according to their DECAPS magnitude. On three panels we plot the binned statistics : median  $\Delta m$ , the interquartile-based measure of the spread of the distribution  $\sigma_G$ , and median photometric uncertainty.

TABLE 8: Listing of pairs of visits at two different epochs, two per density regime. RA and DEC are in degrees. The separation in arcseconds is between the center of each exposure field of view. The last column shows the time difference between the two visits.

visit1	ra1	dec1	magzero1	visit2	ra2	dec2	magzero2	d2d [arcsec]
525904	140.5531	-51.24729	29.47	527300	140.5534	-51.24555	29.459	6.3
525920	143.2337	-51.44724	29.4465	527296	143.2329	-51.446	29.259	4.8
525846	133.5462	-44.27313	29.738	530012	133.5508	-44.27435	29.783	12.6
525879	137.6415	-54.08343	29.775	530032	137.642	-54.08628	29.734	10.3
525837	131.5622	-48.59523	30.011	527246	131.5601	-48.59695	29.699	7.9
525838	132.5935	-50.30486	29.344	527247	132.5894	-50.30705	28.991	12.3
525814	126.4261	-43.06979	29.4545	529974	126.4192	-43.07151	29.466	19.2
525900	140.6165	-48.15003	29.772	529989	140.6162	-48.15212	29.809	7.6

same location, filter and exposure time, but different epoch (see Table 8). This allowed to compare the spread in photometry epoch-to-epoch within DECAPS, and LSST. We illustrate that plotting the magnitude differences on Figs. 16 and 17, and the summary of the spread of photometric difference as a function of magnitude on Figs. 18 and 19.

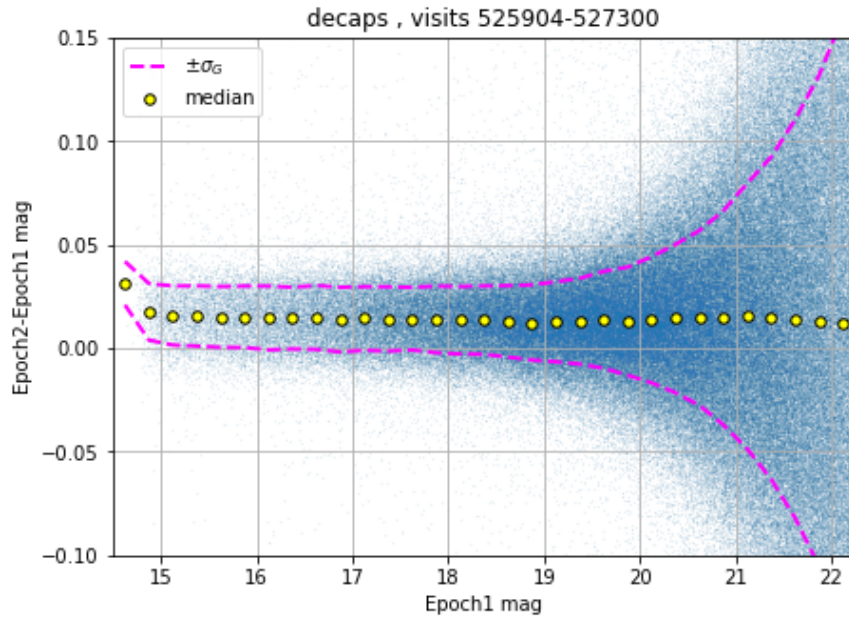


FIGURE 17: Similarly to Fig. 13, scatter plot of the magnitude difference between the two epochal visits (525904, 527300) to the same sky region, separated by 2.95 days, processed by DECAPS. The magnitude difference is shown for all sources cross-matched between the two epochs, with a match within 0.5 arcseconds - there is no selection on magnitude difference, but 0.5 mag (used for completeness) is well beyond the bounds of the plot, and would only cut the outliers to which neither median nor  $\sigma_G$  (interquartile-based estimate of the spread) are not sensitive. We overplot the  $\pm\sigma_G$  envelope, and the median of each of 0.25 mag bins, spread between 14.5 and 22.5 mag.

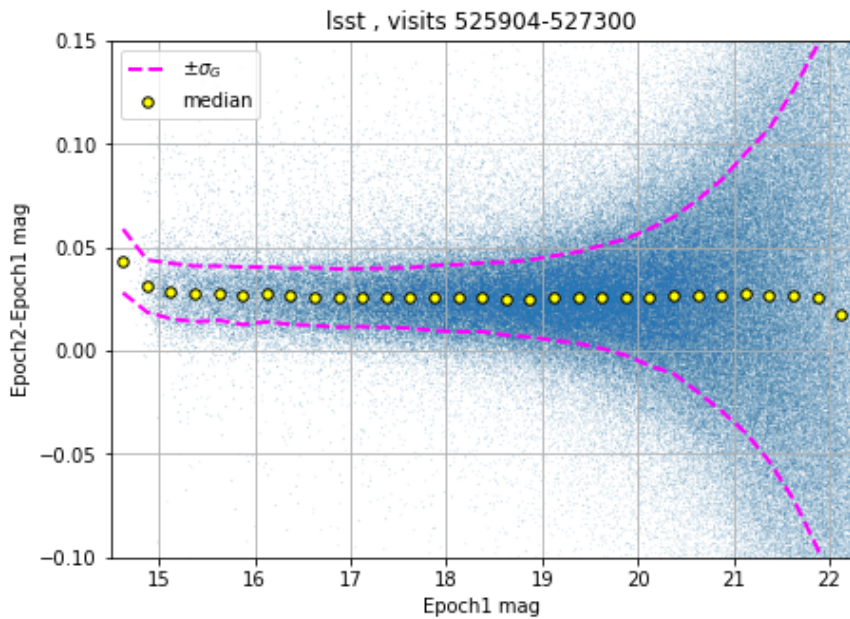


FIGURE 18: The same as Fig. 16, but for LSST processing of two visits to the same region, at two different epochs.

The statistical spread epoch-to-epoch is on the level of 0.1 mag, which is almost twice as large as the spread between processing of the same field by two different pipelines (0.05 mag).

We summarize the information about the photometric repeatability (epoch-to-epoch within a given pipeline), and offset (pipeline-to-pipeline of the same epoch), by combining information from Figs. 18, 19, 15.

## 6 Future work

### 6.1 LSST Processing of StarFast Simulated Sky

An independent way to further test the performance of the LSST Science Pipelines is to use the simulated sky images, where the true position and brightness of each source is known. This would put the measure of source detection completeness, photometric and astrometric precision on an absolute scale. We already tested a StarFast image simulator<sup>9</sup>, and confirmed that it can successfully simulate a region of the sky seeded with known stellar population.

---

<sup>9</sup><https://dmtn-012.lsst.io>

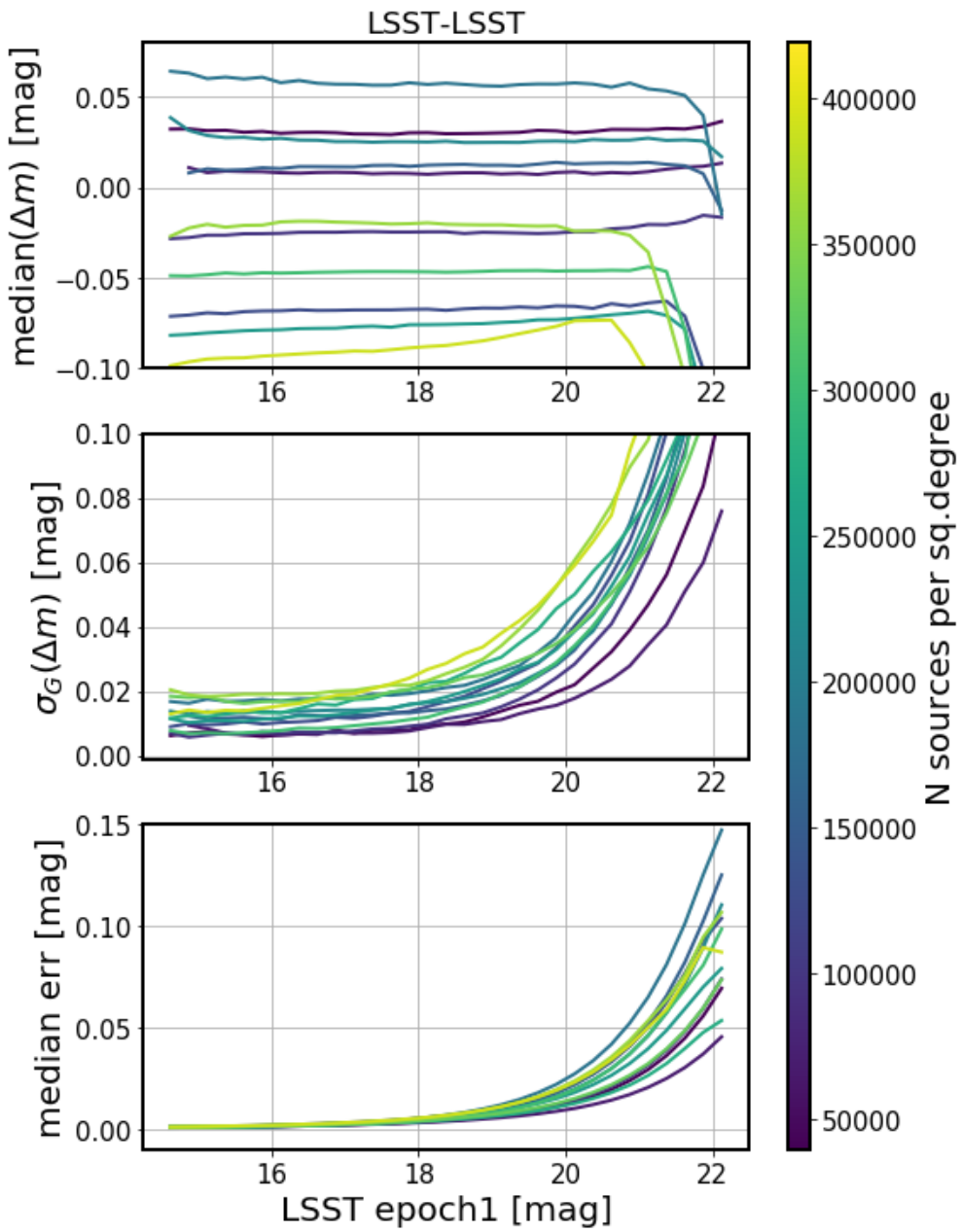


FIGURE 19: The internal repeatability test of the LSST pipeline. We cross-match the source catalogs for each visit. These two brightness measurements for the same source are akin to a two-epoch light curve. Since inherently variable sources constitute a small fraction of all stellar objects, and the majority of stars are not variable, the difference in the measured magnitudes would correspond to the empirical measure of noise. All sources cross-matched within 0.5 arcseconds are binned according to their brightness. On the panels we plot, from top to bottom: median photometric offset, the robust interquartile-based measure of standard deviation  $\sigma_G$ , and the median reported measurement uncertainty.

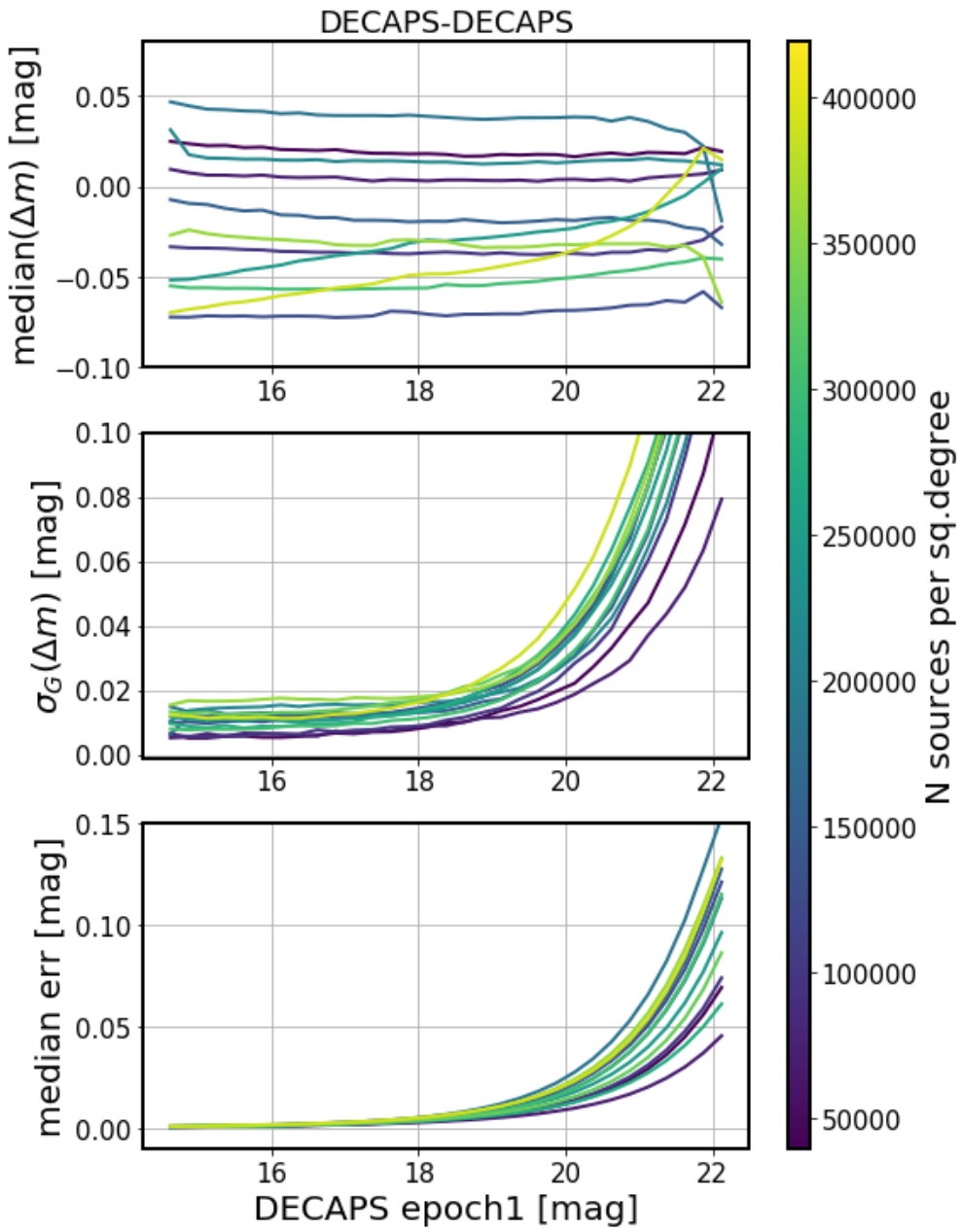


FIGURE 20: The internal repeatability test of DECAPS pipeline - for description, see Fig. 18.

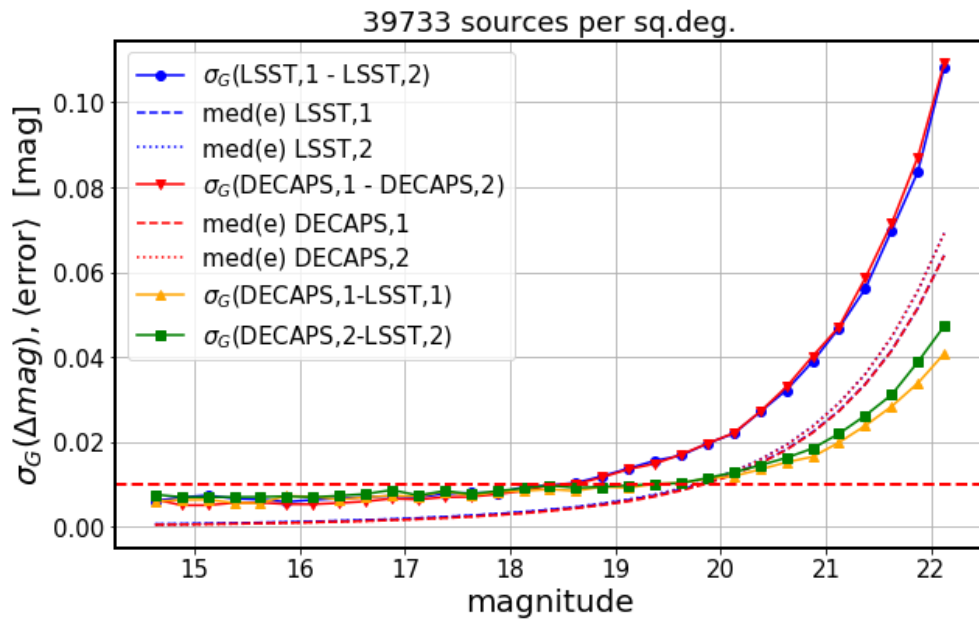


FIGURE 21: Comparison of spread of scatter between two pipelines vs. the empirical measurement of noise from repeatability for a pair of visits at the same location : 525846 and 530012, here called epoch1 and epoch2. All solid lines are  $\sigma_G(a, b)$  - the interquartile-based measure of spread of magnitude difference between measurements  $a$  and  $b$  of the same source. From the top,  $\sigma_G(LSST, 1 - LSST, 2)$ , and  $\sigma_G(DECAPS, 1 - DECAPS, 2)$ , correspond to the empirical measure of noise. The blue line  $\sigma_G(LSST, 1 - LSST, 2)$  is the same quantity as that plotted on the middle panel of Fig. 18, while the red line  $\sigma_G(DECAPS, 1 - DECAPS, 2)$  is the same as that of Fig. 19. Then the dotted and dashed lines in the middle show the median error for epoch 1 or epoch 2, as reported by LSST or DECAPS pipelines. They represent the expected uncertainty in repeated measurement. Since they are identical, the red and blue dotted or dashed lines overlap. Finally, the green and orange solid curves correspond to the scatter between the two pipelines , calculated either for epoch1 ( $\sigma_G(DECAPS, 1 - LSST, 1)$ ), or epoch2 ( $\sigma_G(DECAPS, 2 - LSST, 2)$ ). Fig. 21 shows the second step in the analysis.

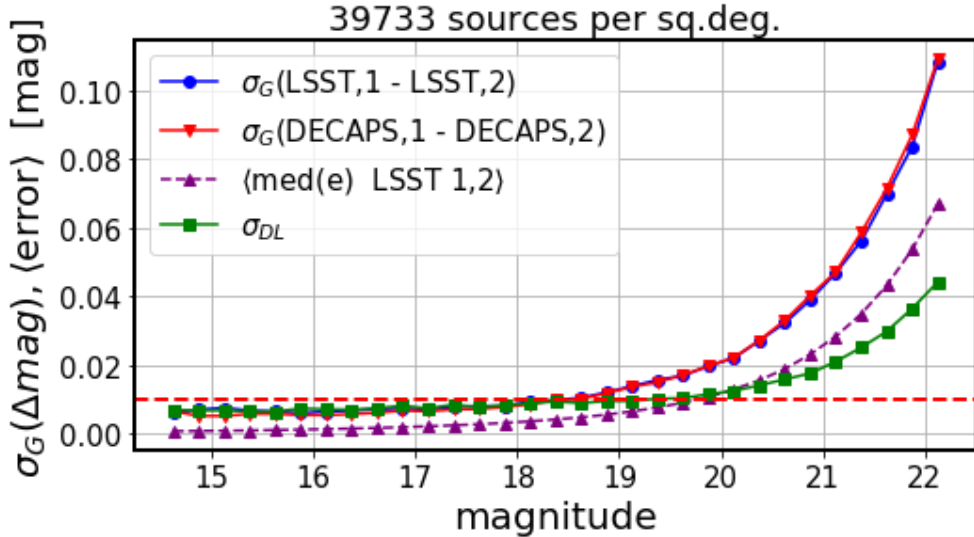


FIGURE 22: Second step in the analysis of photometric spread, following Fig. 20. The blue and red lines of repeatability are unchanged. Since LSST and DECAPS errors are almost identical, we choose to represent the minimum statistical offset by the mean LSST error between the two visits , added in quadrature . If  $e_{1L}$  and  $e_{2L}$  are LSST-reported error measurements for a given source for the two epochs, the quadrature-mean is  $e_{12} = \sqrt{e_{1L}^2 + e_{2L}^2}/\sqrt{2}$ , and the purple dashed line is the median of  $e_{12}$  per magnitude bin. We also add in quadrature the spread between the two pipelines, represented on Fig. 20 by orange  $\sigma_{DL,1}$  for epoch1, and green  $\sigma_{DL,2}$  for epoch2 :  $\sigma_{DL} = \sqrt{\sigma_{DL,1}^2 + \sigma_{DL,2}^2}/\sqrt{2}$ . Note that since the top blue (or red) lines  $\sigma_G(LSST, 1 - LSST, 2)$ ,  $\sigma_G(DECAPS, 1 - DECAPS, 2)$  ( $\sigma_{DD}$ ,  $\sigma_{LL}$  for short) consists of noise  $\sigma_E$  and the systematic offset  $\sigma_S$  :  $\sigma_{LL}^2 = \sigma_S^2 + \sigma_E^2$ . Thus we calculate the systematic offset for LSST as  $\sigma_S = \sqrt{\sigma_{LL}^2 - \sigma_E^2}$ , which is the difference between blue solid and purple dashed lines.

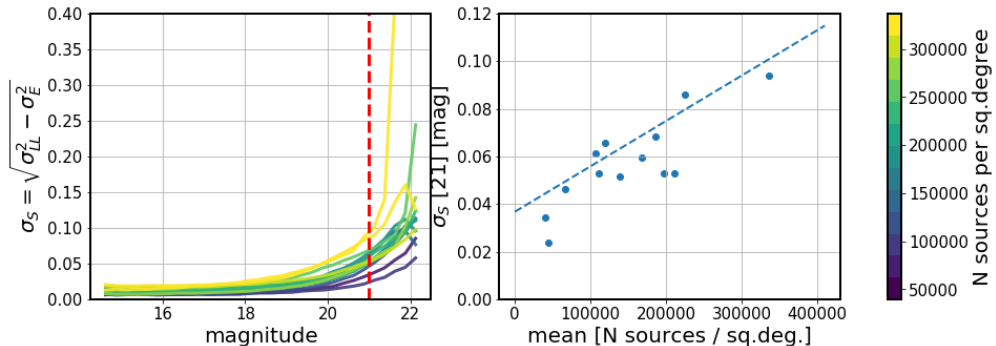


FIGURE 23: The left panel shows the measure of systematic offset between mean photometric error, and the photometric repeatability for the LSST pipeline as a function of magnitude (see Figs. 20, 21. Colors correspond to mean stellar density. Right panel shows  $\sigma_S$  at 21st magnitude as a function of stellar density.

## 6.2 Other LSST-DECAPS tests: w-color

An independent test of the quality of photometry would be to consider the width of the stellar locus ('w-color') on the g-r vs r-i color-color plot. This could be used to test internal consistency of LSST and DECAPS photometry.

## 6.3 Astrometry

Astrometry corresponds to the measurement of the position of sources in an absolute World Coordinate System (WCS). Accurate and precise astrometry enables for instance catalog cross-matching, and over long-term - measurement of proper motion of stellar sources.

We consider two properties of successful astrometry. First, the internal consistency of pipeline by measuring the repeatability of astrometric measurement between different epochs. Second - accuracy, in particular, any possible biases between two different pipelines.

DECAPS used 2MASS and GAIA for the astrometric calibration [9], while LSST Pipelines use the GAIA-TGAS astrometric solution.

We correct the offset in  $\alpha$  :  $\Delta\alpha_{corr} = \delta\alpha \cos(\delta)$

To test repeatability we use pairs of observations at the same location. Fig. 23 shows an example of the LSST-LSST comparison, with Fig. 24 showing the magnitude dependence. Fig. 25 shows the offset in  $RA$ ,  $DEC$ , for DECAPS-DECAPS comparison.

To test possible offset between LSST and DECAPS astrometric solutions, on Fig. 28 we find the offset in measured  $RA$ ,  $DEC$  for sources cross-matched in catalogs from the two pipelines.

## A Appendix A: TRILEGAL and DAOPhot

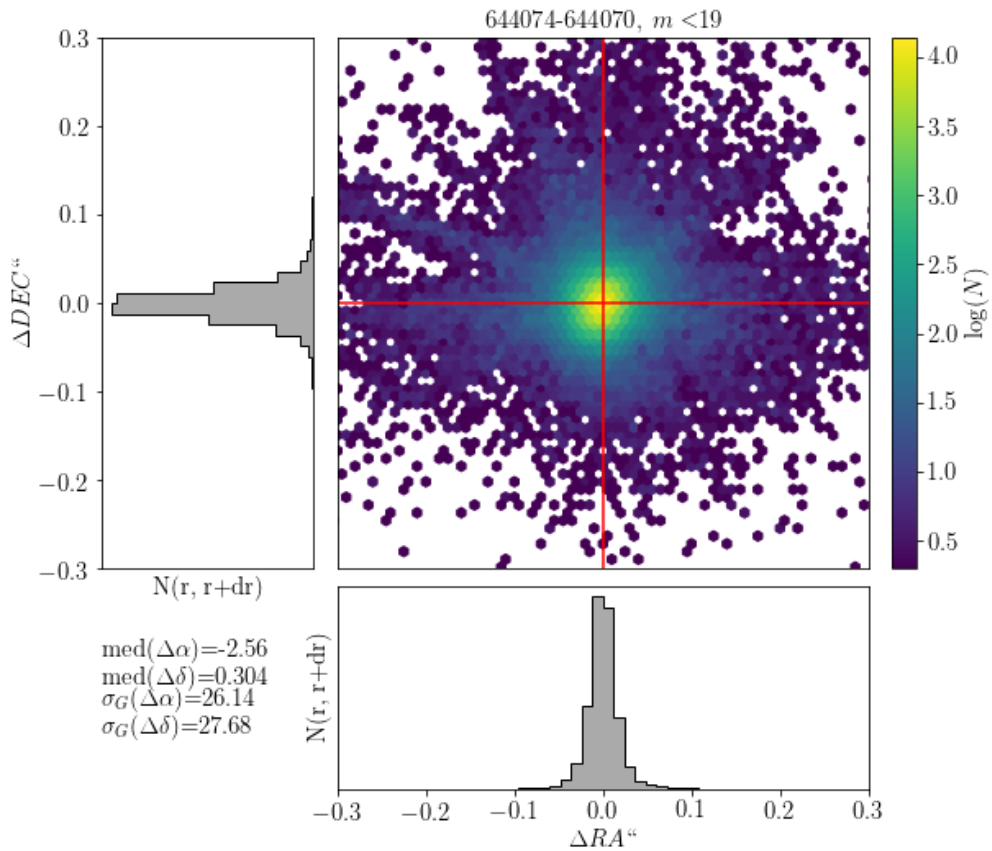


FIGURE 24: The difference of LSST processing for RA,DEC for visits 644074,644070: a pair of visits at the same location, separated by less than a day. The mean number of sources is 419000 sources per sq.deg., which corresponds to top 1% of the sky. We select sources brighter than 19 magnitude. For all other pairs the offsets are all centered on zero with similar spread - see Table 9

LSST processing, visits 644074-644070 mean 419000 sources per sq.deg.

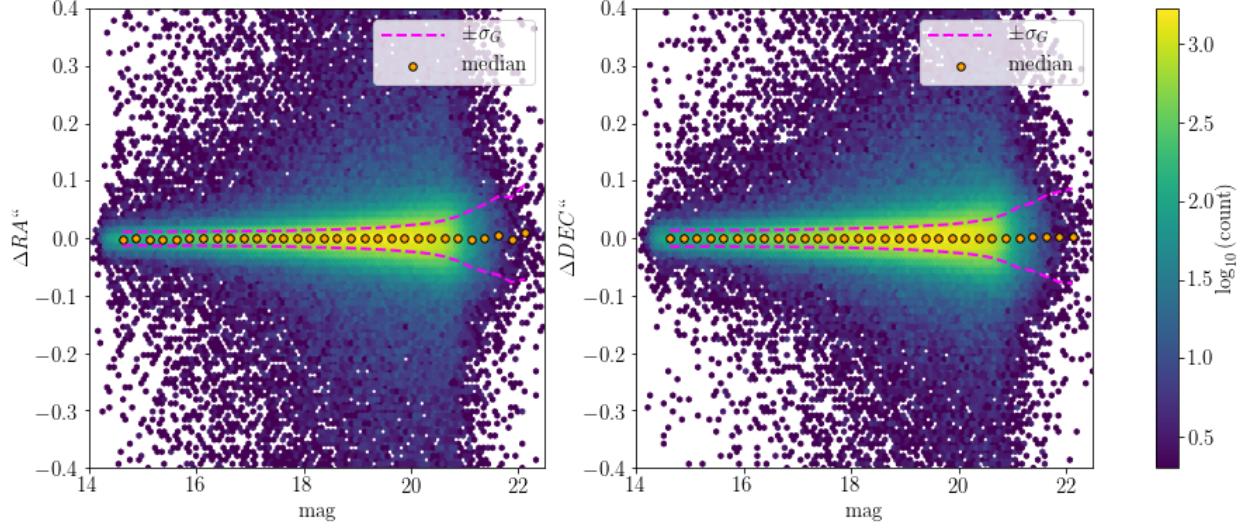


FIGURE 25: The difference in RA,DEC for the same visits as on Fig. 23, shown as a function of magnitude.

TABLE 9: The difference in RA,DEC for various visits, between LSST processing of fields at the same location, but observed at different times ( see Table 8 for summary). The median and spread of astrometric offset are in miliarcseconds. The final column shows the mean source count between the two visits per square degree.

visit1	visit2	med( $\Delta\alpha$ )	med( $\Delta\delta$ )	$\sigma_G(\Delta\alpha)$	$\sigma_G(\Delta\delta)$	$\langle N \rangle$
525846	530012	1.83	0.18	9.43	8.85	39733
525900	529989	-3.12	0.36	10.87	11.58	44577
525814	529974	-0.29	1.15	10.65	10.46	66455
525838	527247	2.52	-2.23	9.96	12.21	94766
525837	527246	1.58	-1.24	9.07	11.51	110734
525920	527296	0.88	-3.2	10.36	9.85	119371
525904	527300	0.43	-1.55	8.29	10.0	138384
641497	644035	2.26	-1.42	19.8	22.68	167267
567283	645255	-5.58	1.05	33.77	19.75	185894
644082	527555	-4.16	-5.05	29.92	26.1	186731
527453	640995	-0.33	1.7	12.95	12.25	195763
525879	530032	0.8	-0.46	10.56	13.41	197058
527064	527552	-0.13	-2.19	16.93	15.74	224731
526028	641500	-1.2	0.42	11.52	11.12	281929
641548	644011	1.2	-2.43	26.08	30.7	336729
644144	566793	1.05	-0.25	27.86	19.69	339183
644074	644070	-2.56	0.3	26.14	27.69	419000

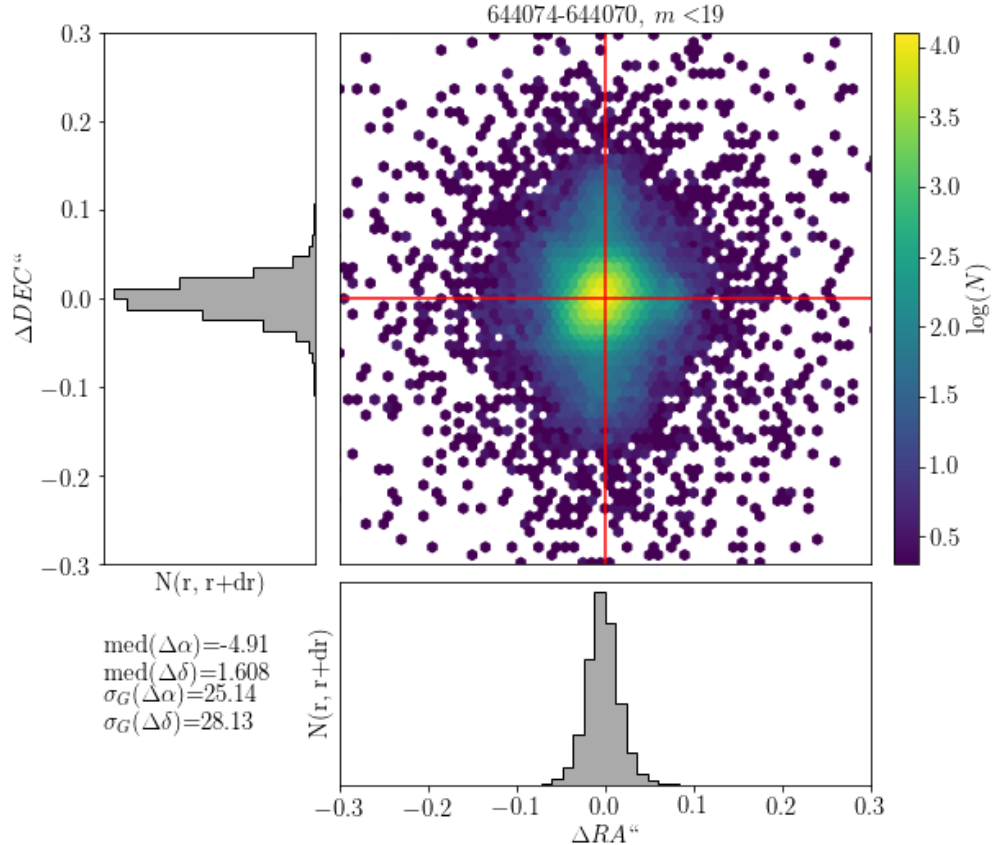


FIGURE 26: The difference in RA,DEC for the same visits as in Fig. 23, but comparing DECAPS single-epoch catalogs. The spread of  $\Delta\alpha$ ,  $\Delta\delta$  is wider than for equivalent visit pairs processed by the LSST Science Pipelines - see Table 10

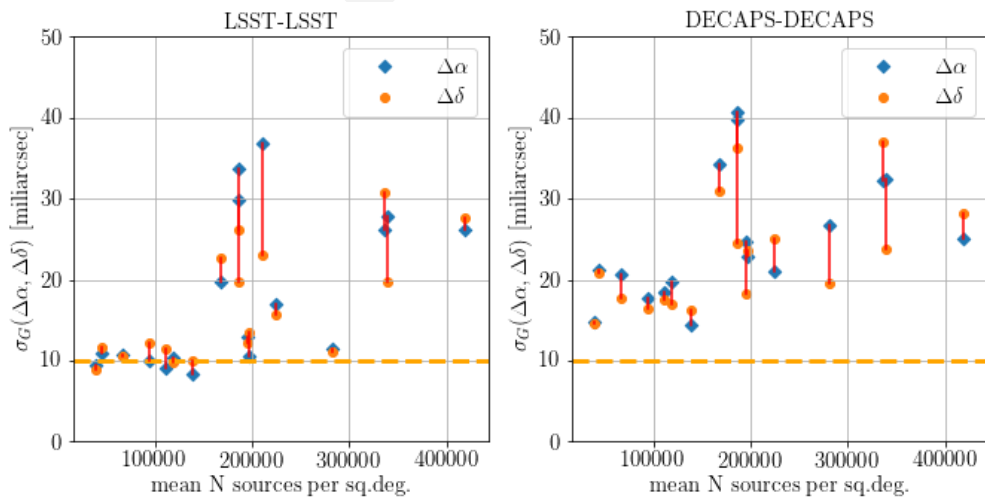


FIGURE 27: Summary of LSST and DECAPS repeatability of astrometry, as in Tables 9 and 10.

TABLE 10: The difference in RA,DEC for various visits, between DECAPS processing of fields at the same location, but observed at different times ( see Table 8 for summary). All measured quantities are in miliarcseconds. See Table 9 for the equivalent visits processed by LSST.

visit1	visit2	med( $\Delta\alpha$ )	med( $\Delta\delta$ )	$\sigma_G(\Delta\alpha)$	$\sigma_G(\Delta\delta)$	$\langle N \rangle$
525846	530012	5.92	-1.18	14.69	14.49	39733
525900	529989	-5.34	-4.18	21.18	20.76	44577
525814	529974	6.55	0.19	20.58	17.76	66455
525838	527247	-6.5	-0.72	17.62	16.45	94766
525837	527246	-3.55	-2.86	18.5	17.57	110734
525920	527296	-4.97	-3.26	19.72	16.88	119371
525904	527300	-5.05	-4.13	14.4	16.26	138384
641497	644035	8.91	12.57	34.18	31.02	167267
567283	645255	-53.12	-49.23	39.71	24.55	185894
644082	527555	139.33	-15.63	40.71	36.27	186731
527453	640995	-126.51	28.81	24.75	18.27	195763
525879	530032	-0.43	-5.17	22.88	23.66	197058
527064	527552	5.11	-3.74	20.95	25.13	224731
526028	641500	-134.26	28.5	26.81	19.56	281929
641548	644011	-1.69	-5.63	32.3	36.95	336729
644144	566793	94.95	68.82	32.42	23.74	339183
644074	644070	-4.92	1.61	25.15	28.14	419000

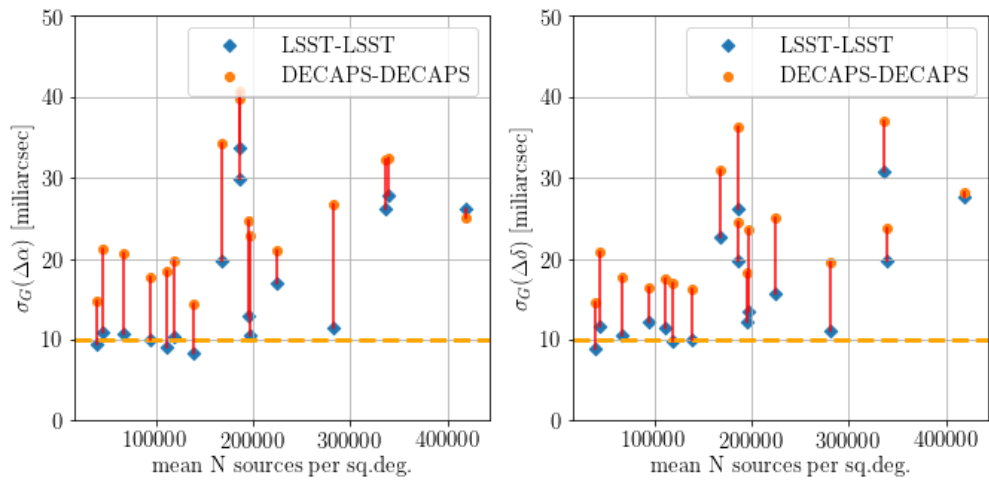


FIGURE 28: Comparison of LSST-LSST, DECAPS-DECAPS on the same scale, data from Tables 9 and 10.

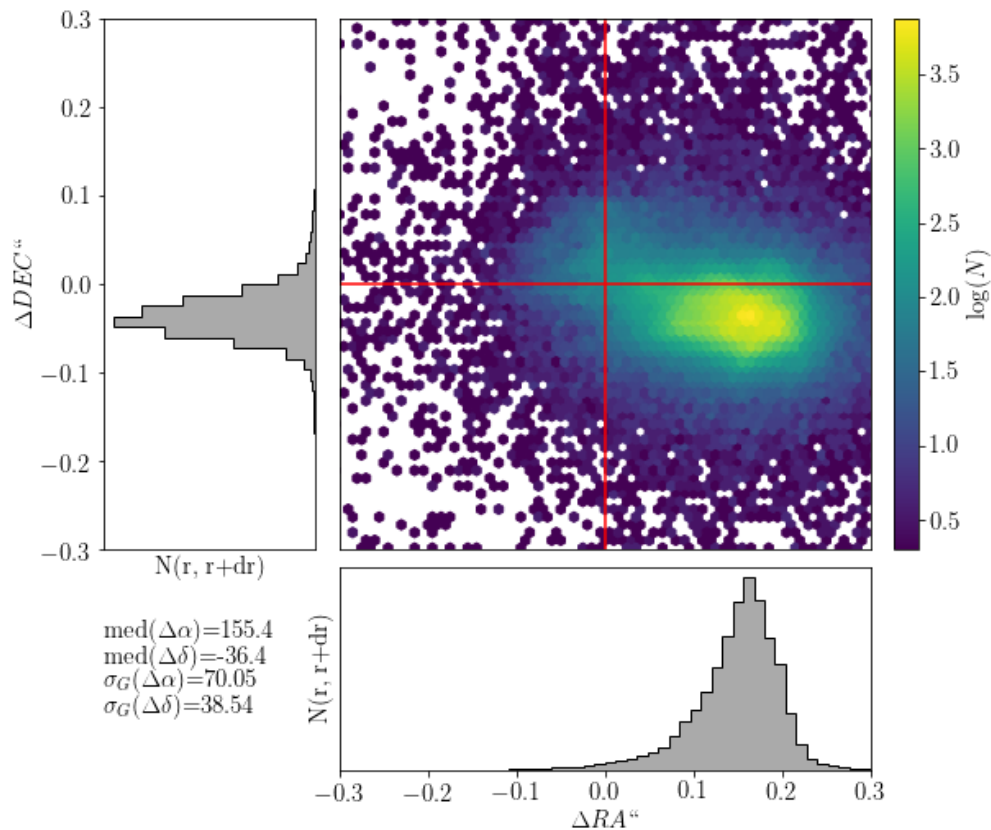


FIGURE 29: The difference in RA,DEC for visit 525904 , between LSST and DECAPS processing (402270 detected sources in the clean LSST catalog ). We tested that for other vists and in all cases the offset position and magnitude remains the same - see Table 11

TABLE 11: The difference in RA,DEC for the same visit analyzed by LSST and DECAPS. Each row corresponds to a separate visit, which correspond to different stellar density. All measured quantities are in miliarcseconds.

visit	median( $\Delta\alpha$ )	median( $\Delta\delta$ )	$\sigma_G(\Delta\alpha)$	$\sigma_G(\Delta\delta)$
525904	155.49	-36.46	70.06	38.55
525920	130.45	-27.53	72.83	43.88
525846	105.62	-51.71	42.49	30.04
525879	131.93	-42.62	138.58	75.68
525837	96.01	-47.93	65.17	36.6
525838	124.9	-68.92	59.56	33.99
525814	39.99	-29.87	47.26	29.72
525900	127.61	-32.38	54.81	33.67
527300	146.26	-38.73	56.49	25.48
527296	120.47	-26.98	41.65	27.14
530012	111.21	-51.38	35.01	28.34
530032	126.69	-47.85	115.02	65.23
527246	88.38	-49.06	45.87	30.6
527247	110.44	-66.18	43.15	29.71
529974	49.13	-30.91	48.55	28.95
529989	126.51	-33.77	52.12	28.33

## A.1 DAOStarFinder source detection

Per each density regime, we performed source extraction with DAOStarFinder<sup>10</sup>. This tool uses a classic DAOFIND algorithm [11], and we used it to verify the plausibility of the MAF source densities using real data. We performed a straightforward DAOPhot source extraction setting the detection threshold at  $5\sigma$  level, setting the detection threshold at  $5\sigma$ .

## A.2 TRILEGAL queries

For the same regions of the sky we also obtained TRILEGAL<sup>11</sup> simulation results, keeping  $r < 24.5$  sources, with all other run settings as default.

## A.3 Comparison of MAF, DAOStarFinder, and TRILEGAL counts

We used the number of sources per TRILEGAL output file, and scaled it to the degree level to compare with MAF and DAO. The results are shown in Tables 12, 13, 14, 15 for 1%,5%,20%

<sup>10</sup><http://photutils.readthedocs.io/en/stable/photutils/detection.html>

<sup>11</sup><http://stev.oapd.inaf.it/cgi-bin/trilegal>

archive	<i>l</i>	<i>b</i>	TRILEGAL	MAF	DAO
c4d_140624_080728_ooi_r	13.70	-4.43	7,960,511	2,650,680	498,760
c4d_170428_094150_ooi_g	356.86	-3.90	39,852,793	4,587,804	375,980
c4d_170501_055757_ooi_g	356.26	5.05	16,352,821	2,659,968	285,630
c4d_170504_084722_ooi_g	4.26	5.15	15,586,874	2,833,740	561,795

TABLE 12: Source density comparison for 1% density level : TRILEGAL, DAO and MAF columns contain stellar counts from TRILEGAL simulation , DAOStarFinder based on DECam data, and MAF simulation, respectively. All counts are in stars per square degree.

and 50 % density levels.

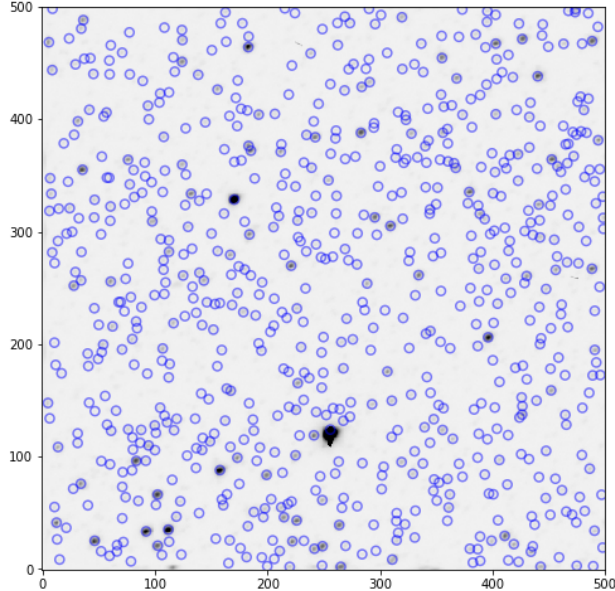


FIGURE 30: 500x500 pixels (135x135 arcseconds) subregion of DECam field c4d\_170504\_084722\_ooi\_g, a top 1% density region. With DAOPhot threshold set at  $5\sigma$ , we detected 722 sources in this postage stamp miniature, corresponding to the area of 0.001406 sq degrees, which translates to 513,422 sources per square degree. At the same coordinates, MAF density is 2,833,740 sources per square degree, and TRILEGAL density is 15,586,874 sources per square degree.

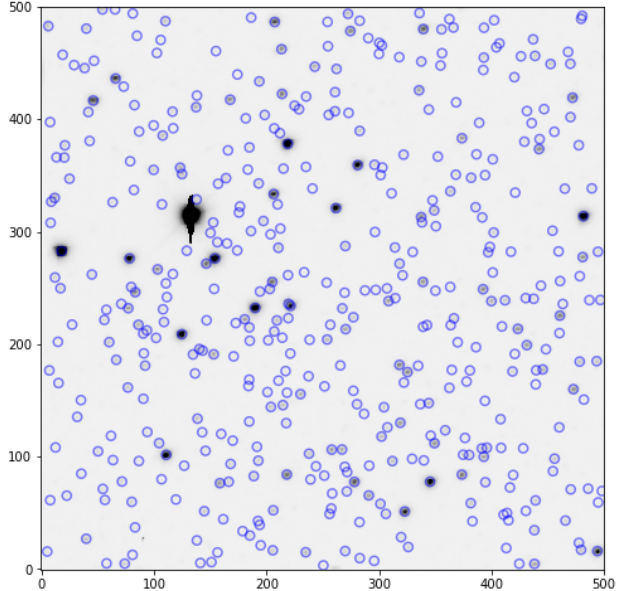


FIGURE 31: 500x500 pixels (135x135 arcseconds) subregion of DECam field c4d\_170429\_035748\_ooi\_g, with 436 detected sources, in the 5 % density region. The same DAOPhot settings as Fig. 29. That many sources in an area of 0.001406 sq degrees, translates to 310,044 sources per square degree. At the same coordinates, MAF density is 807,156 sources per square degree, and TRILEGAL density is 1,870,414 sources per square degree.

## References

- [1] Bosch, J., et al. 2017, ArXiv e-prints

archive	I	b	TRILEGAL	MAF	DAO
c4d_160316_065235_ooi_g	301.42	3.40	1,606,135	591,336	179,277
c4d_160825_231905_ooi_g	314.05	3.08	2,564,964	589,572	127,088
c4d_170429_035748_ooi_g	310.43	-4.02	1,870,414	807,156	327,483
tu1677011	4.48	8.70	2,530,163	810,144	509,093

TABLE 13: Source density comparison for 5% density level, all columns and units as in Table 12

archive	I	b	TRILEGAL	MAF	DAO
c4d_170122_055542_ooi_g	242.43	3.77	341,343	116,856	66,282
tu1661798	351.66	20.42	183,778	118,188	44,216
tu1668579	217.04	1.21	379,319	111,096	54,004
tu2187073	312.84	14.64	184,583	107,784	60,678

TABLE 14: Source density comparison for 20% density level, all columns and units as in Table 12

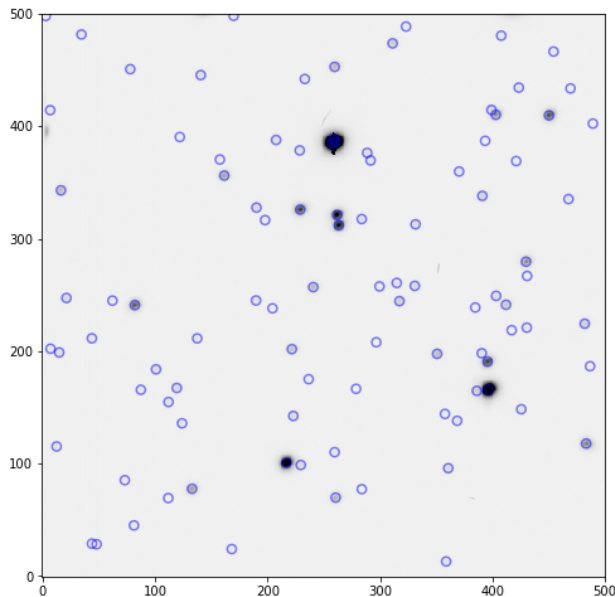


FIGURE 32: 500x500 pixels (135x135 arcseconds) subregion of DECam field c4d\_170122\_055542\_ooi\_g, with 98 detected sources, in the 20 % density region. The same DAOPhot settings as Fig. 29. That many sources in an area of 0.001406 sq degrees, translates to 69,688 sources per square degree. At the same coordinates, MAF density is 116,856 sources per square degree, and TRILEGAL density is 341,343 sources per square degree.

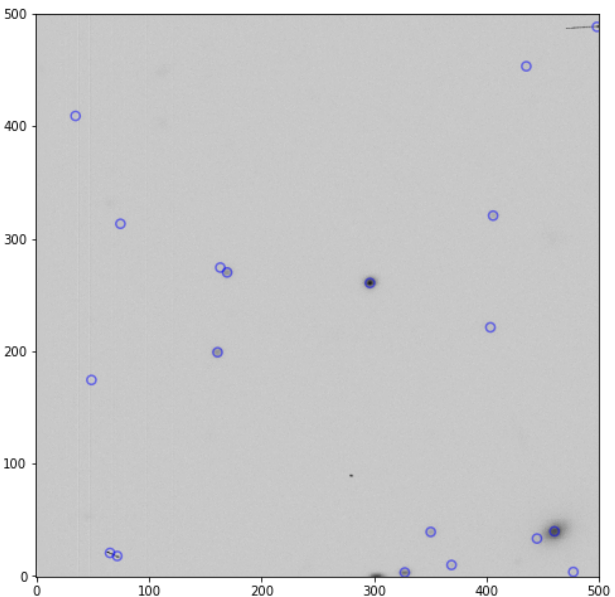


FIGURE 33: 500x500 pixels (135x135 arcseconds) subregion of DECam field c4d\_160607\_025052\_ooi\_g, with 19 detected sources, in the 50 % density region. The same DAOPhot settings as Fig. 29. That many sources in an area of 0.001406 sq degrees, translates to 13,511 sources per square degree. At the same coordinates, MAF density is 20,052 per square degree, and TRILEGAL density is 29,607 sources per square degree.

archive	I	b	TRILEGAL	MAF	DAO
c4d_150615_005257_ooi_g	344.39	41.67	27,633	21,024	12,904
c4d_160607_025052_ooi_g	2.92	41.68	29,607	20,052	13,371
c4d_160825_034122_ooi_g	345.83	1.28	18,364,268	20,268	91,177
tu2046406.fits.fz	220.89	-16.08	41,832	19,944	35,974

TABLE 15: Source density comparison for 50% density level, all columns and units as in Table 12

- [2] Hogg, D. W. 2001, *The Astronomical Journal*, 121, 1207
- [3] Lupton, R. 2005, in prep.
- [4] Lupton, R., Gunn, J. E., Ivezić, Z., Knapp, G. R., & Kent, S. 2001, in *Astronomical Society of the Pacific Conference Series*, Vol. 238, *Astronomical Data Analysis Software and Systems X*, ed. F. R. Harnden, Jr., F. A. Primini, & H. E. Payne, 269
- [5] Lupton, R. H., Ivezić, Z., & Gunn, J. 2005, in prep.
- [6] Lupton, R. H., Ivezić, Z., Gunn, J. E., Knapp, G., Strauss, M. A., & Yasuda, N. 2002, in *SPIE Proceedings*, Vol. 4836, *Survey and Other Telescope Technologies and Discoveries*, ed. J. A. Tyson & S. Wolff, 350
- [7] Narayan, G., et al. 2018, ArXiv e-prints
- [8] Olsen, K. A. G., Blum, R. D., & Rigaut, F. 2003, *AJ*, 126, 452
- [9] Schlaflay, E. F., et al. 2017, ArXiv e-prints
- [10] Shaw, R. A. 2015, *NOAO Data Handbook*
- [11] Stetson, P. B. 1987, *PASP*, 99, 191